Equivalent-circuit modeling of electron-hole recombination in semiconductors and mixed ionic-electronic conductors

Davide Moia ⬤*,†

Department of Physical Chemistry of Solids, Max Planck Institute for Solid State Research, Heisenbergstr. 1, 70569, Stuttgart, Germany

The analysis and optimization of solar energy conversion and light-emitting devices can greatly benefit from equivalent circuit models describing their response. However, a general model of electron-hole recombination in semiconductors is currently missing. This study presents equivalent circuit models of radiative and nonradiative electron-hole recombination processes in the small-signal regime based on their linearized analytical treatment. While resistors accurately describe radiative recombination, bipolar transistors represent the general model of nonradiative recombination, and they can be replaced by resistive elements only in special cases. The proposed recombination model is integrated into a transmission-line circuit representation of complete devices that is equivalent to the linearized drift-diffusion equations in one dimension. For mixed conducting devices, such as halide perovskite solar cells, appropriate simplifications of the complete model provide analytical solutions describing the bulk and interfacial polarization effects that influence the small-signal electrostatics, recombination currents, and overall impedance. The resulting analysis facilitates data interpretation and is relevant to a wide range of materials and devices used for solar energy conversion as well as other optoelectronic and photoelectrochemical applications.

I. INTRODUCTION

This work presents a circuit model that is analytically equivalent to the linearized drift-diffusion equations for semiconductor and mixed ionic-electronic conductor-based devices. The analysis identifies suitable circuit elements describing electron-hole recombination based on the linearized expressions of radiative and nonradiative recombination rates and integrates such elements into a transmission line model. The derivation of practically relevant approximations of such a model is presented. These can be helpful in the experimental investigation of devices, such as solar cells, via small-perturbation methods.

Equivalent circuit models used in conjunction with impedance spectroscopy measurements and other time or frequency-domain (opto)electronic techniques represent a powerful approach to the study of semiconductors and mixed ionic-electronic conductors [1–4]. Transmission-line equivalent circuit models are a physically meaningful starting point for the description of the small-perturbation

response due to transport and storage of charges, applicable to one-dimensional devices close to equilibrium [3,5–8]. For devices such as solar cells and light-emitting diodes under operation, the electron and hole populations are not at equilibrium, requiring appropriate models of the thermal generation and recombination of electronic charge carriers. Resistive elements are commonly used for this purpose [9]. While simple, this approach may not always bear physical correspondence with situations where multiple processes influence the overall electron-hole recombination rate in the semiconductor.

In mixed ionic-electronic conductors, such as hybrid metal-halide perovskites, an additional layer of complexity is introduced by the influence of mobile ionic defects on the recombination dynamics [10–12]. For example, investigation of perovskite solar cells and other mixed conducting devices revealed unphysically large values of capacitance and negative capacitance (inductive behavior) in their impedance at low frequencies, features that have been interpreted based on frequency-dependent electronic processes, such as recombination [13–19].

Ionic-to-electronic current amplification effects can be responsible for such behavior, whereby energy barriers associated with electron-transfer reactions change due to ion redistribution, producing changes in electronic current occurring over "ionic time scales" [13,20–22]. Such an effect concerns recombination processes as well as charge injection at interfaces, giving rise to additional low-frequency impedance features and influencing the apparent

---

*Contact author: moia.davide@gmail.com
†Present address: Fluxim AG, Katharina-Sulzer-Platz 2, 8400 Winterthur, Switzerland.

capacitive and inductive behavior of the device. Attempts to translate such phenomena in equivalent circuit model terms have been made [13,17,20,23–25]. The use of bipolar transistors was introduced to implement the "gating" of the electronic current by the interfacial potential changes associated with the response of an ionic circuit branch. The resulting model could describe much of the optoelectronic behavior of hybrid perovskite solar cells [13]. Another approach consists in fitting empirical *R-C* elements as well as inductive elements to the low-frequency response. While these have no physical meaning, they can be related to the ionic influence on the electronic current [13,17,23,26]. A surface polarization model and a modified polarization model have been suggested as analytical approximations of the drift-diffusion model describing perovskite solar cells [27–30]. The approach succeeded at reproducing impedance spectra with one or two low-frequency features that have been observed experimentally, by considering the role of ionic as well as of electronic charge carriers in the frequency-dependent electrostatic and recombination behavior.

Despite this progress, the connection between currently proposed equivalent circuit models and the analytical description of electron-hole recombination is still missing. For complete devices based on mixed ionic-electronic conductors, the search for appropriate circuit models addressing multiple low-frequency impedance features observed in experiments is still an open question. On a general level, progress in the development of accessible models with analytical solutions that can facilitate experimental data analysis is needed.

This work formalizes the use of resistors and bipolar transistors to describe electron-hole recombination in semiconductors (Sec. III A). Such a description, integrated within a transmission line, results in an analytically accurate model that allows the analysis of bulk and interfacial recombination in one-dimensional semiconducting devices with or without mobile ions (Sec. III B). Based on the implications of typical device structures and bias conditions, the model can be simplified into more accessible versions, for which analytical solutions of practical relevance are derived (Sec. III C). The results exemplify the connection between the complete linearized drift-diffusion model of the problem and simplified circuit models, such as the one proposed in Ref. [13]. Calculated impedance spectra using the proposed models (Sec. III D) point to the relevance of these findings for the description of devices based on hybrid perovskites, as well as other mixed conductors, but also for traditional semiconductors with negligible ionic conductivity.

II. BACKGROUND

This section reviews some basic concepts related to electronic charge-carrier equilibrium and nonequilibrium in semiconductors that will be useful in the remainder of this study. Applying the equilibrium condition to electron-hole thermal generation and recombination in semiconductors leads to the mass-action law

$$n_{\text{eq}}p_{\text{eq}} = K_B. \tag{1}$$

Here, n_{eq} and p_{eq} correspond to the equilibrium electron and hole concentrations and K_B indicates the mass-action constant for the electronic charge carriers (often expressed as the square of the intrinsic electronic charge concentration, n_i^2). Under such conditions, the recombination rate R counterbalances the "thermal" generation rate G_{th}. That is, while $R \neq 0$ and $G_{\text{th}} \neq 0$, the net rate of recombination $U = R - G_{\text{th}}$ is zero. The equilibrium between the electron and hole populations obeys Fermi-Dirac statistics involving a single Fermi level E_F (or electrochemical potential $\tilde{\mu}_{e^-}$).

The application of light or voltage bias takes the semiconductor out of equilibrium, where the electron and hole populations (n and p) obey two separate quasiequilibria. The steady-state situation can be described by the modified mass-action law

$$np = n_i^2 \exp[(V_p - V_n)/V_{\text{th}}]. \tag{2}$$

Here, V_{th} is the thermal voltage, defined based on Boltzmann's constant, temperature and the elementary charge as $V_{\text{th}} = k_B T/q$. The two quasielectrochemical potentials for electrons and holes correspond to $-qV_n$ and qV_p. Here, the use of the symbol V emphasizes their relationship with the "voltages" at the nodes within the equivalent circuit model, as adopted in Refs. [13,31]. These potentials are also indicated with $\tilde{\mu}_n$ and $\tilde{\mu}_p$ in the literature, or expressed in terms of quasi-Fermi-energies (E_{Fn} and E_{Fp}). In Eq. (2), the values of n and p differ from the equilibrium case depending on $q(V_p - V_n)$, which is commonly referred to as quasi-Fermi-level splitting (QFLS).

When different routes for recombination are at play, the total net recombination rate can be expressed as

$$U = \sum_k U_k = \sum_k (R_k - G_{\text{th},k}), \tag{3}$$

where R_k and $G_{\text{th},k}$ are the recombination and the thermal generation contributions of the kth process. Analytical expressions of the net recombination rate associated with radiative, Shockley-Read-Hall (SRH, trap-mediated) and Auger recombination processes [Fig. 1(a)] are available [33,34]:

$$U_{\text{rad}} = k_{\text{rad}}(np - n_i^2), \tag{4}$$

$$U_{\text{SRH}} = \frac{np - n_i^2}{\tau_n(p + p_1) + \tau_p(n + n_1)}, \tag{5}$$

$$U_{\text{Aug}} = \gamma_n(n^2 p - n_{\text{eq}}^2 p_{\text{eq}}) + \gamma_p(np^2 - n_{\text{eq}} p_{\text{eq}}^2). \tag{6}$$
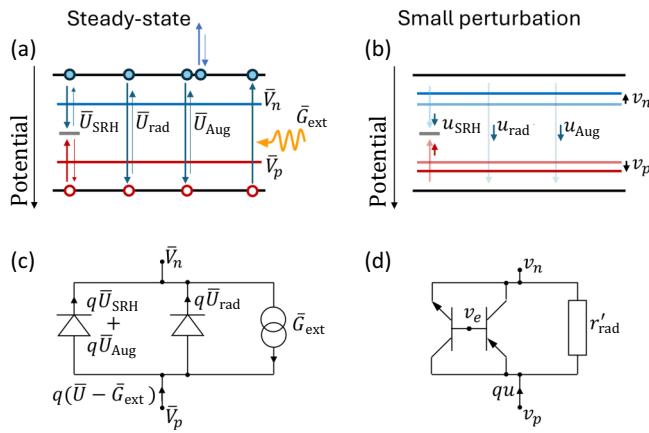
FIG. 1. (a),(b) Energy diagrams representing (a) the steady state and (b) the small-perturbation local recombination and thermal-generation processes occurring in a semiconductor under bias (see text). (c),(d) Equivalent circuit models describing the recombination current per unit volume for (c) the steady state and (d) the small-perturbation regimes. The latter considers only the small electrical perturbation (as it is the case in an impedance experiment) and it involves a resistor $r'_{\rm rad}$ in parallel to an *npn* and a *pnp* bipolar transistor pair. The $q\bar{U}$ and qu terms refer to local net recombination currents per unit volume and the $G_{\rm ext}$ term to the, in this case constant, generation rate per unit volume due to illumination. The ideality factor of the radiative recombination diode is $m_{\rm rad} = 1$. For the Auger and SRH diode, m depends on the operation conditions. A "Potential" y axis is used in (a),(b) to indicate the connection between the potentials in the diagram and in the circuits below (such Potential is connected to the partial free enthalpy of electronic charges [32], often referred to as energy, E).

The parameters $k_{\rm rad}$, γ_n, and γ_p refer to the radiative-rate constant and Auger coefficients of the material, respectively. The terms τ_n and τ_p are carrier capture lifetimes that depend on trap concentration, as well as on the capture cross section and the carrier thermal velocity, while the parameters n_1 and p_1 are defined based on the trap energy position within the band gap E_T [35,36].

In a solar cell, the functional form of Eqs. (4)–(6) dictates the dependence of the net recombination current in the active material when a potential $V_{\rm app}$ applied to the device leads to a position-dependent nonequilibrium condition (QFLS $\neq 0$). This is reflected in the dependence of the total current density flowing in the device, $J_{\rm tot}$, on the applied potential, often discussed in terms of the diode equation:

$$J_{\rm tot} = J_0(e^{V_{\rm app}/(mV_{\rm th})} - 1). \qquad (7)$$

In Eq. (7), J_0 is a saturation current, ==while m is the ideality factor, which encapsulates information on the position and the type of recombination process that dominates $J_{\rm tot}$== [Fig. 1(c)] [34]. In devices, including mixed conductors,

such information is further convoluted with the influence of mobile ionic defects on recombination [23,37,38].

III. RESULTS AND DISCUSSION

A. Equivalent circuit model of recombination processes

The analytical description of recombination presented in the previous section allows the derivation of corresponding equivalent circuit models, through a small-signal analysis of the relevant functions [Figs. 1(a) and 1(b)]. All quantities are presented using a notation ($V = \bar{V} + v$, $J = \bar{J} + j$ or $n = \bar{n} + \tilde{n}$) that identifies the steady state ($\bar{V}, \bar{J}, \bar{n}$) and the (small) deviation from steady state (v, j, $\tilde{n}$). The latter can be caused, for example, by the ac voltage applied to the device when recording impedance spectra. The lower case is used also to identify differential circuit elements used in the model (e.g., small-perturbation resistors and capacitors as r and c, as well as conductance and transconductance terms as g).

The total small-signal net recombination current per unit volume can be expressed, based on Eq. (3), as $qu = \sum_k qu_k$. In view of deriving an appropriate equivalent circuit description of the recombination terms, the analysis focuses on the relation between each contribution, qu_k, and the relevant potentials. The latter are the change in electrochemical potentials of electrons and holes, v_n and v_p, and the change in electrostatic potentials, v_e [Fig. 1(b)], represented as potentials of a small-perturbation circuit network [Fig. 1(d)].

For radiative recombination, linearization of Eq. (4) yields

$$u_{\rm rad} = k_{\rm rad}\bar{n}\bar{p}\left(\frac{\tilde{n}}{\bar{n}} + \frac{\tilde{p}}{\bar{p}}\right). \qquad (8)$$

The change in carrier concentration can be expressed based on the small-signal chemical potential of electrons, $v_{\mu,n} = v_e - v_n$, and holes, $v_{\mu,p} = v_p - v_e$. It follows that $\tilde{n} = \bar{n}(v_e - v_n)/V_{th}$ and $\tilde{p} = \bar{p}(v_p - v_e)/V_{th}$, yielding

$$qu_{\rm rad} = \frac{v_p - v_n}{r'_{\rm rad}}. \qquad (9)$$

Here, $r'_{\rm rad} = V_{th}/qk_{\rm rad}\bar{n}\bar{p}$ is interpreted as a recombination resistor connected between the nodes associated with v_p and v_n [Fig. 1(d)]. $r'_{\rm rad}$ has units of $\Omega\,{\rm cm}^3$, that is the inverse of a conductance per unit volume. Of note, the change in electrostatic potential v_e does not appear in Eq. (9), as radiative recombination scales linearly with the product of the electron and hole concentrations.

For the Shockley-Read-Hall recombination rate, linearization of Eq. (5) yields

$$u_{\text{SRH}} = \frac{\tau_n \bar{p}(\bar{p} + p_1) + \tau_p \bar{p} n_1 + \tau_p n_i^2}{[\tau_n(\bar{p} + p_1) + \tau_p(\bar{n} + n_1)]^2} \tilde{n}$$
$$+ \frac{\tau_p \bar{n}(\bar{n} + n_1) + \tau_n \bar{n} p_1 + \tau_n n_i^2}{[\tau_n(\bar{p} + p_1) + \tau_p(\bar{n} + n_1)]^2} \tilde{p}. \quad (10)$$

This expression accurately describes u_{SRH}, if the trapping and detrapping processes involved in the SRH model are at quasiequilibrium (valid for time scales that are slower than the dominant time constant controlling such processes). Again, to describe Eq. (10) in terms of an equivalent circuit model, the small-signal changes in electronic charge carrier concentrations ($\tilde{n}$ and $\tilde{p}$) are expressed as a function of the relevant small-signal electron and hole chemical potentials. In this case, the change in electrostatic potential v_e is involved in the resulting expression of the small perturbation net recombination current per unit volume.

$$qu_{\text{SRH}} = \frac{q}{V_{\text{th}}} \left\{ \frac{\bar{n}\bar{p}[\tau_n(\bar{p} + p_1) + \tau_p n_1]}{[\tau_n(\bar{p} + p_1) + \tau_p(\bar{n} + n_1)]^2}(v_e - v_n) + \frac{\tau_n \bar{p} n_i^2}{[\tau_n(\bar{p} + p_1) + \tau_p(\bar{n} + n_1)]^2}(v_p - v_e) \right.$$
$$\left. + \frac{\bar{n}\bar{p}[\tau_p(\bar{n} + n_1) + \tau_n p_1]}{[\tau_n(\bar{p} + p_1) + \tau_p(\bar{n} + n_1)]^2}(v_p - v_e) + \frac{\tau_p \bar{n} n_i^2}{[\tau_n(\bar{p} + p_1) + \tau_p(\bar{n} + n_1)]^2}(v_e - v_n) \right\}. \quad (11)$$

Equation (11) is arranged to emphasize the contribution of four terms. These, consistent with the description in Ref. [13], can be interpreted as the current contributions due to transconductance terms of *npn* and *pnp* bipolar transistors (with current gain $\beta \to \infty$). The transistors are appropriately connected to the nodes associated with the small-signal electrostatic and quasielectrochemical potentials, as shown in Fig. 1(d) (see Sec. S1 within the Supplemental Material [39] for more details on this representation). On this basis, Eq. (11) can be expressed as follows:

$$qu_{\text{SRH}} = g'_{\text{rec},n}(v_e - v_n) - g'_{\text{gen},n}(v_e - v_p)$$
$$+ g'_{\text{rec},p}(v_p - v_e) - g'_{\text{gen},p}(v_n - v_e). \quad (12)$$

Here, $g'_{\text{rec},n}$ and $g'_{\text{rec},p}$ are electron-hole recombination transconductance terms, while $g'_{\text{gen},n}$ and $g'_{\text{gen},p}$ are (thermal) generation transconductance terms. Each of these parameters is dependent on the specific steady-state condition (the values of $\bar{n}$ and $\bar{p}$), as shown in Eq. (11). The symbol g' represents a recombination transconductance per unit volume (units of A V^{-1} cm^{-3}). The treatment above provides an analytical justification to the use of the bipolar transistor in the modeling of small-perturbation local net recombination described with the Shockley-Read-Hall rate.

The expressions describing transconductance terms can be simplified, depending on the relative magnitudes of $\bar{n}$ and $\bar{p}$, and on the trap's properties. The analysis in Appendix A shows that for the case of shallow traps, and for the case of deep traps with $\tau_n \bar{p} = \tau_p \bar{n}$, one obtains

$g'_{\text{rec},n} \approx g'_{\text{rec},p}$ (assuming similar capture lifetimes for electrons and holes). If such values are referred to as g'_{rec}, and thermal generation can be neglected, it is possible to simplify the expression of qu_{SRH} in Eq. (12) to obtain $qu_{\text{SRH}} = g'_{\text{rec}}(v_p - v_n)$, where v_e is no longer involved. This encourages the definition of a recombination resistance:

$$r'_{\text{SRH}} = 1/g'_{\text{rec}}. \quad (13)$$

In other cases, the transistor representation may be simplified by considering only the current contribution of the transistor type (*npn* or *pnp*) associated with the recombination limiting carrier type (*n* or *p*). This corresponds to the minority carrier, if τ_n and τ_p are of similar magnitude, while different trends are obtained based on Eq. (11) if these parameters are very different from each other. These aspects are discussed in Sec. S2 within the Supplemental Material [39] (including Ref. [40]), where the expressions for the generation transconductance terms are also presented (these have negligible contribution under light and/or forward voltage bias).

Finally, linearization of the Auger net recombination expression leads to

$$qu_{\text{Aug}} = q(2\gamma_n \bar{n}\bar{p} + \gamma_p \bar{p}^2)\tilde{n} + q(2\gamma_p \bar{n}\bar{p} + \gamma_n \bar{n}^2)\tilde{p}. \quad (14)$$

The small-signal net recombination once again depends on each of the carrier concentrations. Similarly to the case of the trap-mediated SRH recombination rate, the change in electrostatic potential appears explicitly in the functional form and an analogous approach to the one used for u_{SRH} can be applied. However, in this case, the generation of

charge carriers is a constant term and does not appear in the small-perturbation treatment (see Sec. S3 within the Supplemental Material [39]):

$$qu_{\text{Aug}} = \frac{q}{V_{\text{th}}}[2\gamma_n \bar{n}\bar{p}(v_e - v_n) + \gamma_n \bar{n}^2(v_p - v_e)$$
$$+ 2\gamma_p \bar{n}\bar{p}(v_p - v_e) + \gamma_p \bar{p}^2(v_e - v_n)]$$
$$= g'_{\text{rec},n}(v_e - v_n) + g'_{\text{rec},p}(v_p - v_e). \quad (15)$$

In summary, a pair of *npn* and *pnp* transistors with appropriate thermal generation (SRH) and recombination (SRH + Auger) transconductance values combined with a radiative resistor [Fig. 1(d)] is an analytically accurate description of the local small-signal net recombination. Such a conclusion is general for any semiconductor (with or without mobile ions), given the fact that the proposed analogy between the linearized transistor equations and the linearized nonradiative SRH and Auger recombination rates is valid at a fundamental level.

The total small-signal net recombination per unit volume can be expressed as

$$qu = \sum_k (g'_{\text{rec},k} v_{\text{rec},k} - g'_{\text{gen},k} v_{\text{gen},k}), \quad (16)$$

or more explicitly as

$$qu = g'_{\text{rec,rad}}(v_p - v_n) + g'_{\text{rec},n}(v_e - v_n) - g'_{\text{gen},n}(v_e - v_p)$$
$$+ g'_{\text{rec},p}(v_p - v_e) - g'_{\text{gen},p}(v_n - v_e), \quad (17)$$

where each contribution involves the product of a recombination (trans)conductance, $g'_{\text{rec},k}$, and a recombination voltage (driving force), $v_{\text{rec},k}$, or the product of a thermal generation transconductance, $g'_{\text{gen},k}$, and a thermal generation voltage, $v_{\text{gen},k}$. Here, the radiative conductance per unit volume is defined as $g'_{\text{rec,rad}} = r'_{\text{rad}}{}^{-1}$, while the recombination transconductance for SRH and Auger processes are combined in $g'_{rec,n}$ and $g'_{rec,p}$.

B. Generalized transmission-line equivalent circuit model

The recombination elements described above can be included within a small-perturbation model of a one-dimensional device, where the local charge-carrier dynamics is coupled to long-range effects [2,41]. Figure 2(a) shows the equivalent circuit model for a device where a mixed ionic-electronic conducting active layer is sandwiched between ion-blocking contacts. The circuit consists of electronic rails for electrons and holes, one ionic rail for the one mobile ionic species considered in this case, and the electrostatic rail. Each rail is drawn along a position axis, x. This circuit allows the evaluation of the changes in (quasi)electrochemical potentials of electrons, holes and ions (v_n, v_p, and v_{ion}) due to the applied small

perturbation (v_{app}) as a function of position, encapsulating properties related to the transport, reaction and storage of charges in the material. As for the change in the electrostatic potential (v_e), this is determined at each position by an interplay between dielectric contributions and the local change in net charge. In the discretized model, resistors and (trans)conductance terms are no longer defined per unit volume (r' in $\Omega\,\text{cm}^3$ and g' in $\text{AV}^{-1}\,\text{cm}^{-3}$), but per unit area ($r$ in $\Omega\,\text{cm}^2$ and g in $\text{AV}^{-1}\,\text{cm}^{-2}$), reflecting their contribution to the recombination current density (A cm^{-2}) flowing in the device.

Before describing the circuit in more detail, it is helpful to discuss the steady-state properties of such a model device, which are used to derive the value of the relevant circuit elements. Given an applied voltage bias ($\bar{V}_{\text{app}}$) and electron-hole generation profile due to light absorption ($G_{\text{ext}}(x)$), the steady-state solution is obtained by solving the Nernst-Planck-Poisson problem (NPP or drift-diffusion model). This yields the values of the electrochemical potential for the electronic ($\bar{V}_n, \bar{V}_p$) and for the mobile ionic charges ($\bar{V}_{\text{ion}}$), as well as the value of the electrostatic potential ($\bar{V}_e$, here associated with the electronic vacuum level profile), as a function of position. These are schematically represented in an ionic and electronic energy diagram in Fig. 2(b) [32], for the case of a solar cell with a mixed conducting active layer and under forward bias. In the diagram, the difference between the value of $\bar{V}_e$ at the left and the right boundary of the full device corresponds to $\bar{V}_{\text{app}} - \phi_{bi}$ where ϕ_{bi} is the built-in potential of the complete stack (difference in work function between the two contact layers, assumed to be doped). $\bar{V}_e$ is determined by Poisson's equation. Its profile depends on the charge distribution in the device, which is dictated by the concentration of fixed charges and of mobile charge carriers, and by the ability of the latter to screen electric fields. Such screening occurs over a distance on the order of the Debye length, L_D (for small perturbations of the local potential). In the case of a mixed conductor with one monovalent mobile ionic species, L_D is defined as

$$L_D = \sqrt{\frac{\epsilon V_{\text{th}}}{q \sum_{j=n,p,\text{ion}} n_{j,\text{bulk}}}}, \quad (18)$$

where ϵ is the dielectric constant of the material and $n_{j,\text{bulk}}$ is the bulk charge concentration of carrier j ($j = n, p, \text{ion}$). The value of L_D is dominated by the mobile majority charge carrier(s). Variations in the steady-state profile of $\bar{V}_e$ are largely confined to space-charge regions of width on the order of the material's L_D or wider, depending on whether the majority carrier is accumulated or depleted at such interface [42]. The space-charge potentials developing in the contact and active-layer interfacial regions are indicated in Fig. 2(b) as $\bar{\phi}_A$, $\bar{\phi}_B$, $\bar{\phi}_C$, and $\bar{\phi}_D$. The electrochemical potentials $\bar{V}_n$, $\bar{V}_p$, and $\bar{V}_{\text{ion}}$ complete the steady-state picture. Their position with respect
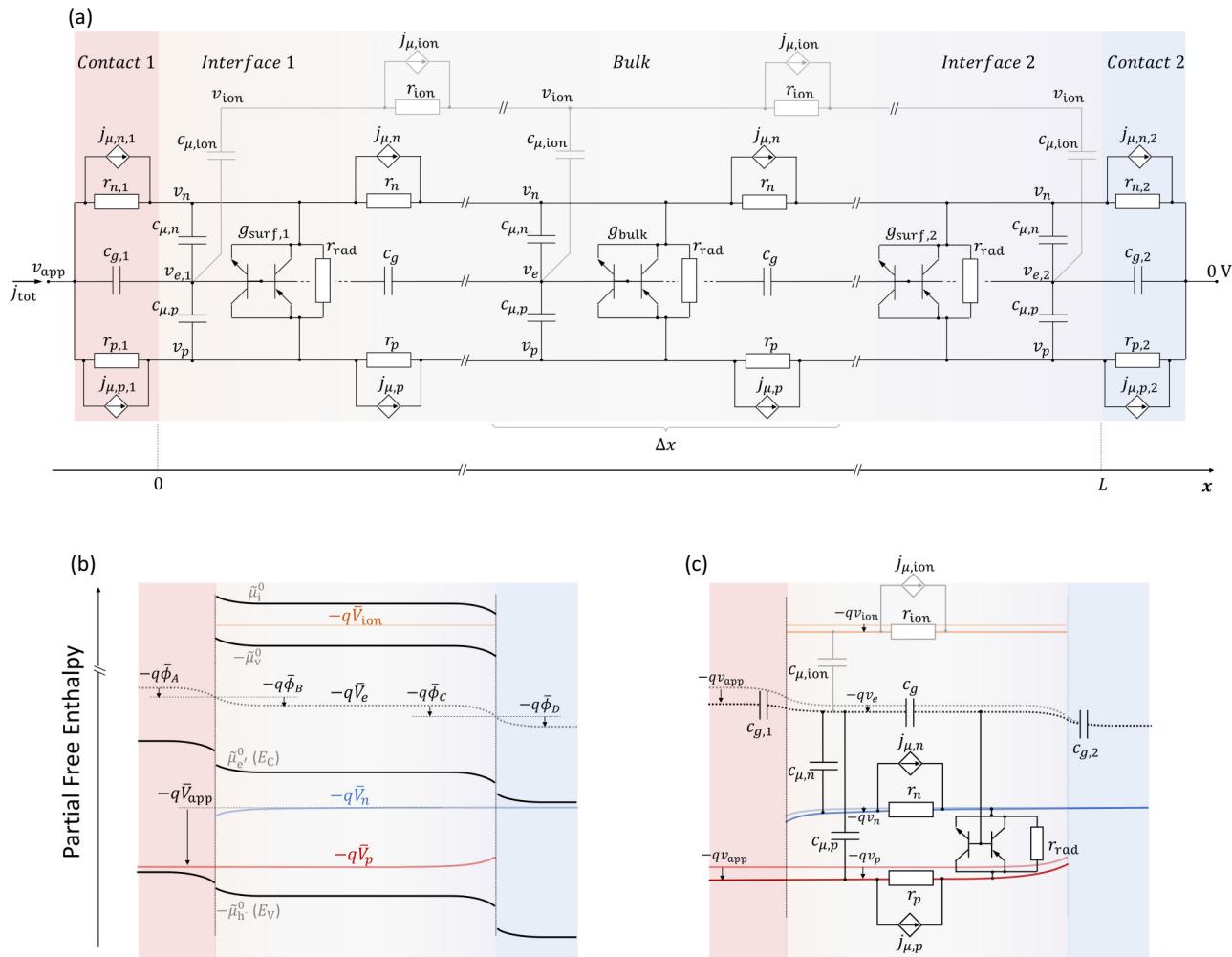
FIG. 2. (a) Equivalent circuit model for a mixed ionic-electronic conductor of thickness L (electrons, holes and one mobile ionic species are considered) between ion-blocking contacts (contact 1 and 2). The model is valid for devices with selective contacts (for each contact either of the electron or hole resistance is very large). The x axis represents the qualitative position in the device, with L being the active-layer thickness. Within the "slice" Δx of the mixed conductor, the model used for the bulk properties is shown (see text). (b) Generalized energy diagram [32] for a mixed conductor based solar cell between selective contacts ($r_{n,1} \rightarrow \infty$ and $r_{p,2} \rightarrow \infty$) under bias (e.g., under light and/or forward voltage $\bar{V}_{app}$) showing the steady-state potentials described in the text. The diagram includes two ionic defects, while in this study only one mobile ion is considered. (c) Schematics illustrating the construction of the equivalent circuit in (a) based on the relation between the small-signal potentials in the energy diagram and their representation in the circuit. The relevant voltages at the circuit's nodes are not the absolute potential values, but their changes with respect to the steady state.

to their corresponding standard potentials $\tilde{\mu}^0$ and their slope provide information on the local steady-state charge concentrations and current components in the device.

Based on the steady-state solution, the circuit elements relevant to the small-perturbation problem can be derived (see Sec. V for details). The electrochemical resistors [7] and the voltage controlled current sources [41] (r_j, and $j_{\mu,j}$, respectively, with subscript $j = n, p, $ ion) describe the linearized charge transport equation. The small-signal current flowing in the resistors is driven by changes in the relevant quasielectrochemical potential gradient (gradient in v_j along the charge-carrier rail). The

current flowing in the controlled sources is sensitive to changes in the charge-carrier chemical potential, according to $j_{\mu,j} = g_{\mu,j} v_{\mu,j}$, where $g_{\mu,j} = \bar{J}_j / V_{th}$ represents a transport transconductance ($\bar{J}_j$ is the steady-state current density associated with species j). The dielectric capacitors (c_g) account for the short-range dielectric properties, while the chemical capacitors [7] ($c_{\mu,j}, j = n, p, $ ion) describe the storage of each of the mobile-charged species in the material. The generation-recombination elements connected between the rails associated with electrons and with holes complete the circuit describing the active layer (transistors with transconductance g_{rec} and g_{gen}, and radiative

recombination resistors r_{rad}). The current flowing through each of these differential circuit elements is driven by the changes in the electrochemical and electrostatic potentials [see schematics in Fig. 2(c)].

The elements in the circuit implement a discretized version of the continuum differential problem. Their value is position dependent [e.g., $r_n = r_n(x)$], based on the local steady-state solution. In Fig. 2(a), such position dependence is not shown for the circuit elements and potentials, for simplicity. Only for the SRH recombination parameters, the circuit emphasizes that these are, in general, different at the interface with the contacts (g_{surf}) compared with the bulk (g_{bulk}) of the active layer. This is due to differences in the values of τ_n, τ_p, n_1, and p_1, besides n and p, as well as to possible recombination contributions involving electronic charges in the contacts.

This study focuses on devices with ion-blocking contacts. These are described in Fig. 2(a) with resistors ($r_{p,1}$, $r_{n,1}$, $r_{p,2}$, and $r_{n,2}$), voltage-controlled current sources ($j_{\mu,p,1}$, $j_{\mu,n,1}$, $j_{\mu,p,2}$, and $j_{\mu,n,2}$), and with the geometric capacitors, $c_{g,1}$ and $c_{g,2}$. These parameters refer to the transport in and capacitance of the space-charge regions at the interfaces on the contact layers' side. This is an approximation, which is valid only for selective contacts (i.e., for each contact layer either $r_n \rightarrow \infty$ and $g_{\mu,n} \rightarrow 0$ or $r_p \rightarrow \infty$ and $g_{\mu,p} \rightarrow 0$) with negligible electronic charge carrier generation due to optical absorption. Accurate treatment of both electrons and holes in the contacts requires recombination elements also in these regions, including the explicit description of the electrostatic potential in transmission-line terms, as shown in the circuit in Fig. S3 within the Supplemental Material [39]. Such a circuit, is referred to as the "complete model" below. An additional series resistance is expected in practical cases, and it is omitted in Fig. 2, for simplicity. If the steady-state ionic current is zero ($\bar{J}_{ion} = 0$), all $g_{\mu,ion} = 0$ and $j_{\mu,ion}$ current source elements can be omitted from the model. Ion penetration in the contacts could also be described by extending the ionic rail throughout the device stack. Finally, the same circuit model without the ionic rail describes devices based on semiconductors without mobile ions.

Note that a complete treatment of the electronic and ionic charge-carrier chemistry may include any possible redox reaction through which not only immobile (as in the traditional SRH treatment) but also mobile ionic defects interact with electrons and holes. This influences the electronic recombination and transport dynamics, but also establishes more complex (quasi)equilibria involving the electronic and ionic defects. In the small-signal picture, these reactions can be represented via circuit elements connecting the electronic and ionic rails [2,31]. This work neglects their contributions, while a more detailed discussion of the nonequilibrium defect chemistry of mixed conductors will be the subject of a separate study.

The frequency-dependent complex impedance of the circuit in Fig. 2(a) is calculated according to

$$Z(\omega) = \frac{v_{app}}{j_{tot}(\omega)} \ . \tag{19}$$

Here, v_{app} is the amplitude of an applied sinusoidal (small) voltage perturbation at angular frequency ω, and $j_{tot}(\omega)$ is the (complex) current density flowing in the circuit at the node of the applied potential [Fig. 2(a)]. The value of $j_{tot}(\omega)$ can be evaluated, for example, by solving the system of linear equations obtained from Kirchhoff's current law applied to all nodes of the circuit minus one. The value of $Z(\omega)$ obtained using the circuit in Fig. 2(a) corresponds to the impedance of the modeled system at the steady-state condition used to derive the values of the circuit elements. Due to the complexity of the analytical solution to this problem, approximated versions of the model are desirable. Possible approaches to this question are presented in the next section.

C. Role of electrostatic potential and approximated models for bulk and interfaces

The contribution of electrostatic effects to the device's electrical response is often described through the overall geometric capacitor of the device in parallel to the remaining components of the equivalent circuit model. However, as evident from the model in Fig. 2(a), this approximation is not applicable in the general case. In particular, the model highlights the following points: local changes in the electrostatic potential, v_e, can have a first-order influence (1) on the nonradiative recombination rate (transistor elements) and (2) on the electronic charge-transport currents ($j_{\mu,j}$ current sources), requiring an explicit account of their gating effect. (3) Due to the connection of the electrostatic rail to the chemical capacitors in the circuit, charge carriers that are high in concentration (high chemical capacitance $c_{\mu,j}$, $j = n$, p, ion) are expected to influence v_e the most. It is useful to discuss the relevance of (1)–(3) in practical situations. The case of devices with efficient electronic charge transport and ion-blocking contacts with opposite selectivity is considered in detail in the following section (relevant to solar cells). In this case, changes in applied potential v_{app} are reflected in equal changes in ($v_p - v_n$) throughout the device. Such a condition might not apply, in general, to measurements performed on solar cells, especially when far from open-circuit conditions [43,44].

1. Semiconductors without mobile ions

First, let us consider the significance of treating explicitly the electrostatic potential in the description of recombination in semiconducting devices with no mobile ions. For this, the transmission-line model in Fig. 2(a), but

without the ionic rail, is the relevant and analytically accurate equivalent circuit model describing the small-signal behavior.

As discussed above, the transistor-based circuit couples the electron-hole recombination current to the electrostatic potential. Such coupling becomes negligible, and the transistor can be well approximated with a suitable r_{SRH} resistor, only in the case of shallow traps, and in the case of deep traps for $\tau_n \bar{p} \approx \tau_p \bar{n}$. Interestingly, a similar approximation can be made in situations involving deep traps and $\tau_n \bar{p} \neq \tau_p \bar{n}$, based on the following argument. If the electron and hole concentrations are very different from each other, e.g., $\bar{p} \ll \bar{n}$, it is reasonable to expect also $c_{\mu,p} \ll c_{\mu,n}$. Given the low impedance associated with the large $c_{\mu,n}$, under the small-perturbation regime and for $\omega > 0$, the approximation $v_e \approx v_n$ can be used. It follows that the single transistor indeed behaves once again like a resistor (in this example, $r_{\text{SRH}} = 1/g_{\text{rec},p}$, see Fig. S4 within the Supplemental Material [39]).

The use of bipolar transistors to describe the SRH recombination rate in semiconducting optoelectronic devices, while formally accurate, can be reasonably approximated with recombination resistors when looking at many practical situations [see model in Fig. 3(a), where efficient electronic transport and selective contacts are also considered]. Only in the case of deep traps, $\bar{p} \approx \bar{n}$ and $\tau_n \bar{p} \neq \tau_p \bar{n}$, is the transistor description needed. Influence of the change in local electrostatic potential on the recombination current is expected in such cases despite negligible ion transport in the device, an aspect that deserves future investigation.

An analytical solution to the impedance of the circuit in Fig. 3(a) is available (see Appendix B). This can be interpreted as a simplified zero-dimensional circuit model consisting of an equivalent capacitance (c_{eq}) and a total recombination resistance ($r_{\text{rec,tot}}$) connected in parallel [Fig. 3(b)]. A similar approach has been discussed in previous studies on solar cells, including the treatment of

electronic transport limitations and of contributions from the contacts [45–47].

The term c_{eq} is often interpreted as the parallel of a total electrostatic capacitance $c_{g,\text{tot}} = \left(c_{g,1}^{-1} + c_{g,2}^{-1} + \sum c_g^{-1}\right)^{-1}$ and a total electronic chemical capacitance $c_{\mu,\text{eon,tot}} = \sum \left(c_{\mu,n}^{-1} + c_{\mu,p}^{-1}\right)^{-1}$. The discussion in Appendix B shows that this is a good approximation in many cases and that the definition of a capacitive term $\hat{c} = c_{\text{eq}} - c_{g,\text{tot}}$ can be used to extract information on the effective electronic contribution to the capacitance ($\hat{c}$, like $c_{g,\text{tot}}$ and $c_{\mu,\text{eon,tot}}$, describes the whole device). Such contribution can be chemical in nature ($\hat{c} \approx c_{\mu,\text{eon,tot}}$), while interfacial space charge contributions can become significant if $c_{\mu,n}$ and $c_{\mu,p}$ are very different (e.g., low-injection condition in a doped semiconductor-based device).

2. Semiconductors with mobile ions

The following discussion focuses on devices where a mixed ionic-electronic conductor is used as the active layer of a solar cell, such as the ones based on halide perovskites. The analytical treatment of the full model is complex, even when considering ideal selective contacts and fast electronic transport (see Sec. S6.2 in the Supplemental Material [39]).

Different approximations of the model can be derived depending on which charge carrier(s) play a significant role in the determination of the electrostatics. To address this question quantitatively, it is helpful to refer to the Debye length defined for each carrier type j as $L_{D,j} = \sqrt{\epsilon V_{\text{th}}/qn_{j,\text{bulk}}}$. Because $L_{D,j}$ refers to the individual carrier screening length, $L_{D,j} < L$ or $L_{D,j} > L$ indicates whether carrier j contributes significantly to the determination of the electrostatic landscape in the active layer or not.

In many cases of interest, the ionic charge-carrier concentration is large enough, such that $L_{D,\text{ion}} \ll L$. As a result, whenever the recombination transistor elements

(a)

(b)
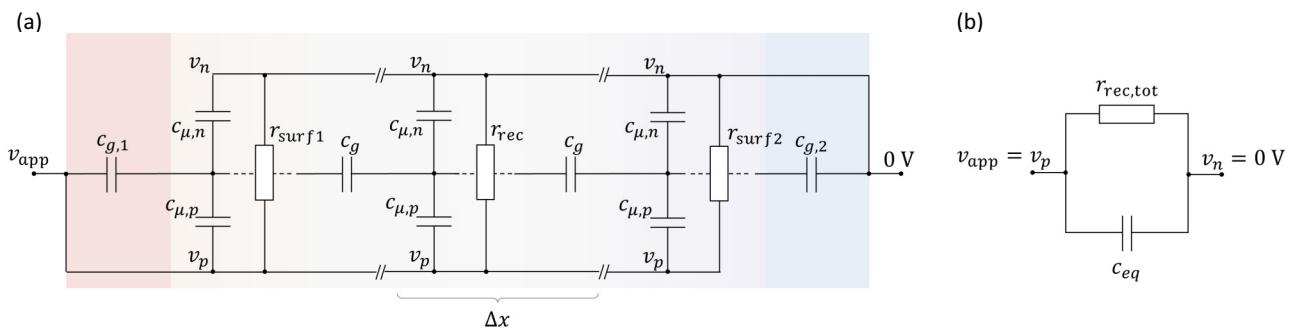
FIG. 3. (a) Simplified version of the transmission-line model for a device based on a semiconductor without mobile ions, assuming that all recombination processes can be modeled as resistors, the rate of electronic transport is significantly faster than the rate of recombination, and ideal contact selectivity (holes for contact 1 and electrons for contact 2). (b) Simplified version of (a), where $r_{\text{rec,tot}} = \left[\left(\sum r_{\text{rec}}^{-1}\right) + r_{\text{surf},1}^{-1} + r_{\text{surf},2}^{-1}\right]^{-1}$, while c_{eq} is the equivalent capacitance of the circuit in (a), which includes the electrostatic and the chemical contributions (see Appendix B).

cannot be reduced to resistors, the ionic situation is key to the electronic response, and the electrostatic rail needs to be considered explicitly [see point (1) above]. Assuming $L_{D,\text{ion}} \ll L$, two scenarios are discussed depending on whether also for at least one of the electronic charge carriers $L_{D,j} < L$, $j = n$, p (see also discussion in Ref. [29]). This is equivalent to stating that not only the ionic chemical capacitance but also the chemical capacitance associated with at least one of the electronic charge-carrier types is large enough to influence the local changes in electrostatic potential [point (3) above].

IC (ion conductor) approximation (*valid for* $L_{D,\text{ion}} \ll L$, $L_{D,n} \gg L$ *and* $L_{D,p} \gg L$). In a first scenario, the steady-state electronic charge concentrations are small enough so that their corresponding Debye lengths are larger than the active-layer thickness (i.e., their ability to screen electric fields is negligible over length scales in the order of L). Equivalently, this means that the total chemical capacitance of the active layer associated with either electrons or holes is small compared with its geometric capacitance ($c_{\mu,n}$ and $c_{\mu,p}$ present a large impedance and can be neglected). This allows one to evaluate the electrostatic-ionic behavior using an "ion conductor" (IC) approximation, independently from the electronic properties of the active layer.

The total current density can be written as the sum of an ionic-electrostatic component and of an electronic component [$j_{\text{ion},e}$ and j_{eon}, respectively, see Fig. 4(a)], $j_{\text{tot}}(\omega) = j_{\text{ion},e}(\omega) + j_{\text{eon}}(\omega)$. Based on Eq. (19), this leads to

$$Z(\omega) = \frac{v_{\text{app}}}{j_{\text{eon}}(\omega) + j_{\text{ion},e}(\omega)} = [Z_{\text{eon}}(\omega)^{-1} + Z_{\text{ion},e}(\omega)^{-1}]^{-1},$$

(20)

where the electronic and the ionic-electrostatic impedance are defined as

$$Z_{\text{eon}}(\omega) = \frac{v_{\text{app}}}{j_{\text{eon}}(\omega)}$$

and

$$Z_{\text{ion},e}(\omega) = \frac{v_{\text{app}}}{j_{\text{ion},e}(\omega)},$$

respectively.

Figure 4(a) shows the resulting equivalent circuit model, for a situation where the condition $v_p(x,\omega) - v_n(x,\omega) = v_{\text{app}}$ (fast electronic transport) is also valid. By neglecting the g_{gen} terms (device under forward and/or light bias), and by integrating both SRH and Auger terms in one set of recombination transconductance parameters, one obtains

$$Z_{\text{eon}}(\omega) = \left\{ \frac{L}{r'_{\text{rad}}} + i\omega\hat{c} + \int_0^L \left[\frac{v_e(x,\omega)}{v_{\text{app}}} g'_{\text{rec},n}(x) \right.\right.$$
$$\left.\left. + \left(1 - \frac{v_e(x,\omega)}{v_{\text{app}}} \right) g'_{\text{rec},p}(x) \right] dx \right\}^{-1}.$$

(21)

Equation (21) includes a frequency-independent radiative term, and a frequency-dependent contribution due to non-radiative recombination. For the latter, the small-signal electrostatic potential modulates the SRH and Auger terms across the device. Of note, $v_e(x,\omega)/v_{\text{app}}$ is obtained from analysis of the ionic-electrostatic circuit, independently of the electronic branch. The $\hat{c}$ element, connected between the nodes corresponding to v_p and v_n, accounts for the electronic capacitive contribution, similarly to the discussion in the previous section. Indeed, while $c_{\mu,n} \ll c_{\mu,\text{ion}}$ and $c_{\mu,p} \ll c_{\mu,\text{ion}}$ based on the assumption in this first scenario, $\hat{c}$ can become relevant at high frequencies, for situations where its value approaches the capacitance due to the electrostatic term (Appendix B).

Replacing the ionic-electrostatic circuit branch in Fig. 4(a) with the one displayed in Fig. 4(b) is a further approximation leading to simple expressions for $Z_{\text{ion},e}(\omega)$ and $Z_{\text{eon}}(\omega)$, and therefore $Z(\omega)$ [Eqs. (C1)–(C6)]. In Fig. 4(b), the small-perturbation potentials dropping across the space-charge capacitors c_B and c_C refer to the changes in the values of ϕ_B and ϕ_C, respectively. Also, $c_{g,1}$ and $c_{g,2}$ are renamed as c_A and c_D to reflect the nomenclature of potentials in Fig. 2(b). The replacement of $c_{\mu,\text{ion}}$ with short circuits ($v_e \approx v_{\text{ion}}$) is valid for large enough values of such capacitance and for nonzero angular frequencies. Note that a solution is available also for the circuit in Fig. 4(a), but only when considering a flat-band situation (Sec. S6.3 within the Supplemental Material [39]).

This approach allows one to explicitly account for the frequency dependence of recombination at all positions in the bulk of the active layer and at the surfaces, extending the concept of ionic-to-electronic current amplification introduced in Ref. [13] to processes occurring across the whole device. Note that in its simplest form [$Z_{\text{ion},e}$ evaluated with the circuit in Fig. 4(b)], the model does not account for recombination across the space charges explicitly (more on this in Sec. V).

Finally, further simplifications to the model can be obtained in special cases. Figure 4(c) shows a circuit with focus on the interfacial behavior, and where the spatial dependence of bulk properties is no longer explicitly described. Here, the r_{ion} and c_g bulk elements in Fig. 4(c) have been replaced with a single parallel circuit involving the total bulk ionic resistance and geometric capacitance ($r_{\text{ion,bulk}}$ and $c_{g,\text{bulk}}$). In addition, the bulk nonradiative recombination and radiative recombination elements are combined within a resistor $r_{\text{rec,bulk}}$. This approximation can be relevant to real devices, either because of the conditions discussed in the previous section (shallow traps, or $\tau_n \bar{p} \approx \tau_p \bar{n}$ throughout the bulk, see Appendix A), or because of negligible dependence of the total bulk recombination current on the small-signal electrostatic potential.

Regarding the interfacial transistor elements, the circuit in Fig. 4(c) shows some differences with the four-transistor circuit proposed in Ref. [13]. These are related
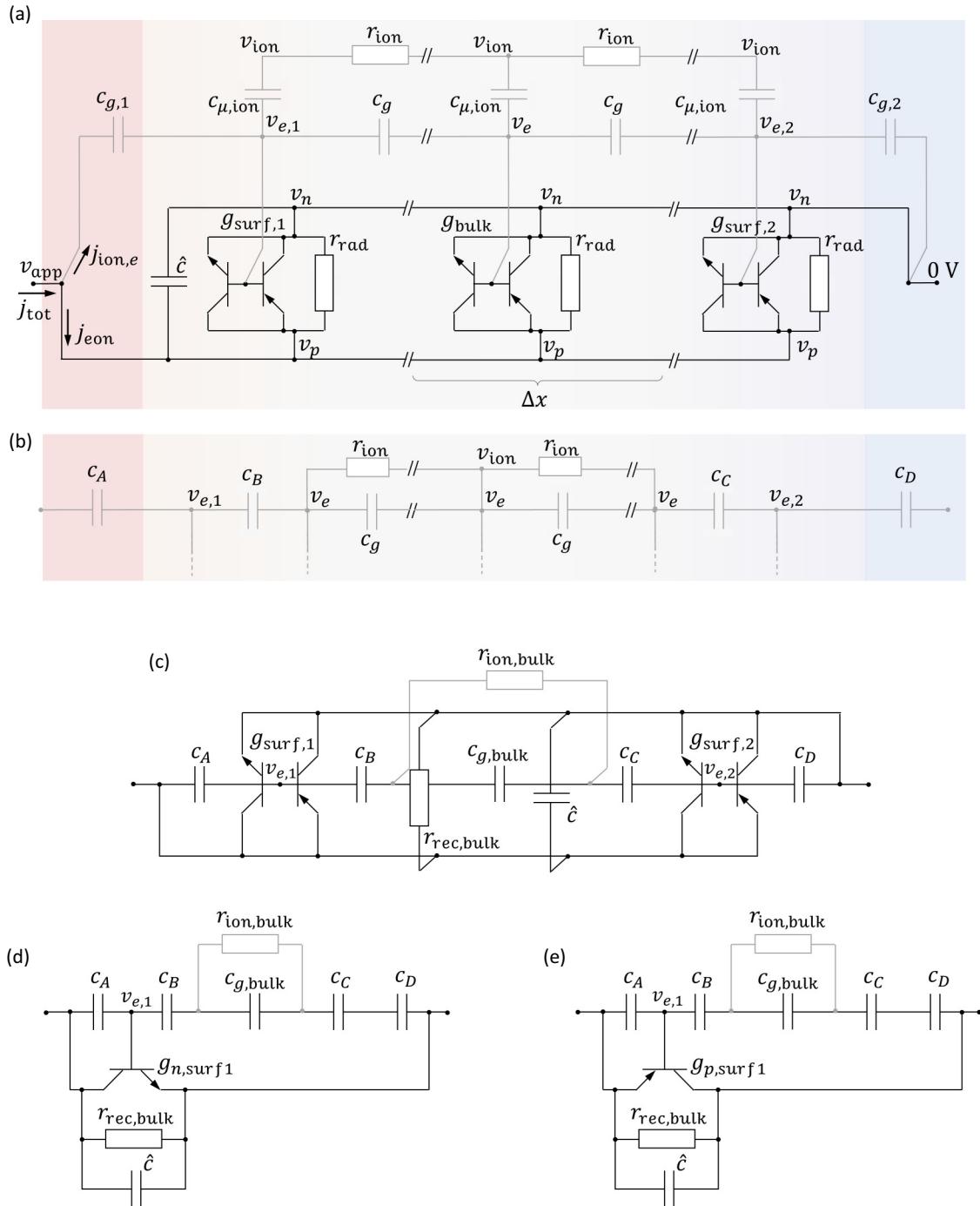
FIG. 4. Ionic conductor approximation for the treatment of the electrostatic potential in a mixed conducting solar cell. (a) Simplified model obtained from Fig. 2(a), by neglecting the electronic chemical capacitors ($L_{D,n} \gg L$ and $L_{D,p} \gg L$). Infinite electronic charge-carrier mobility limit and ideal contact selectivity (holes for contact 1 and electrons for contact 2) are assumed. (b) Further approximation of the electrostatic and ionic rails (see text and Appendix C). In (c)–(e), the network of r_{ion} and c_g elements in (b) is summarized in $r_{ion,bulk}$ (bulk ionic resistance) and $c_{g,bulk}$ (bulk geometric capacitance). The bulk nonradiative and radiative recombination elements are combined within a resistor $r_{rec,bulk}$ (see text). The models include (c) all four transistors describing the recombination at the two interfaces; (d),(e) only one (dominant) transistor for the cases where recombination due to (d) electrons or (e) holes minority carriers at the interface with the hole injecting contact (contact 1) dominates the total recombination current.

to the description of local surface recombination and generation, included in this work, and of electronic charge-transfer reactions across interfaces, neglected here while

considered in Ref. [13]. The interested reader is referred to Sec. S7 within the Supplemental Material for a detailed analysis [39]. One observation from such a discussion is

that the model for an injection-limited situation is in fact analogous to the model of a device where the dominant recombination at an interface involves the charge-carrier type injected from the contact at such an interface as the minority carrier. These conditions lead to low-frequency inductive behavior, as will be shown in the next section.

When evaluating the circuit in Fig. 4(c) for most practical situations, one transistor (the one with the largest value of the product $g_{rec}v_{rec}$) is sufficient to describe the small-signal electronic response of the device under bias. In Figs. 4(d) and 4(e) such a simplification is displayed, for the case where the recombination of the minority-carrier electrons or holes, respectively, at the hole-injecting interface dominates the electrical response (the models described in Refs. [13,48] are recovered, see Appendix C for impedance evaluation). The elements $r_{rec,bulk}$ and $\hat{c}$ can still be included to complete the model.

In all models shown in Fig. 4, the low-frequency time constant of the ionic-electrostatic circuit describes the space-charge polarization process, whereby redistribution of mobile ions at interfaces through the bulk of the active layer and electronic charges in the contacts charge and discharge the interfacial capacitors. This time constant can be expressed as $\tau^{\perp} = r_{ion,bulk}c^{\perp}$, where $c^{\perp}$ is the series of c_A, c_B, c_C, and c_D, and it represents the characteristic time of the slow ionic and electronic currents in the device operating in the IC approximation regime [13,27,31,48–50]. $\tau^{\perp}$ depends on the properties of the active layer ($r_{ion,bulk}$, c_B and c_C) and also of the contacts (c_A and c_D).

MC-i (mixed conductor with mobile ions as majority carriers) approximation (*valid for $L_{D,ion} \ll L$, $L_{D,ion} \ll L_{D,p}$ and $L_{D,ion} \ll L_{D,n}$*). The second scenario relaxes the assumption of low electronic charge concentration. It can describe also situations where one or both electronic carrier types contribute significantly to the determination of the electrostatics in the active layer, while mobile ions remain the majority carriers. This condition is relevant to the modified surface polarization model presented by Clarke *et al.* [28,29]. Such large steady-state concentrations for at least one of the electronic charge carriers are obtained if large enough (voltage and/or light) bias is applied to the mixed conducting device. Note that, unlike semiconductors with

no mobile ions, the condition $\bar{p} \neq \bar{n}$ in the bulk of mixed conductors is the norm rather than the exception, even at large biases (see Sec. S8 within the Supplemental Material [39]). The condition $L_{D,p} > L$ and/or $L_{D,n} > L$ may be met also for small bias, if very thick samples are considered (large L), or if the charge carrier equilibrium due to material and device preparation leads to large enough values of $\bar{n}$ or $\bar{p}$ in the bulk (e.g., intrinsic or extrinsic doping). In equivalent circuit modeling terms, this means that the electron and/or the hole chemical capacitance is large, so that the ionic-electrostatic circuit impedance and the function $v_e(x,\omega)/v_{app}$ cannot be calculated separately from the electronic circuit, as was the case in the IC approximation.

Aiming to obtain a model with an analytical solution also in this case, the transmission line shown in Fig. 2(a) is simplified as follows. Chemical capacitors associated with the neutral component (see Ref. [2] and Fig. S15 within the Supplemental Material [39]) that couple either electrons or holes with the ionic rail are defined:

$$c_n^{\delta} = \frac{c_{\mu,ion}c_{\mu,n}}{c_{\mu,ion} + c_{\mu,n}}, \quad (22)$$

$$c_p^{\delta} = \frac{c_{\mu,ion}c_{\mu,p}}{c_{\mu,ion} + c_{\mu,p}}. \quad (23)$$

Note that the voltage dropping across $c_{\mu,j}$ capacitors ($j = n,p,$ion) is the small-signal chemical potential of the individual jth charge. On the other hand, the voltage dropping across c_j^{δ} refers to the small-signal quasichemical potential of the neutral species (defined by the ionic and jth electronic charge carrier), which is related to changes in local stoichiometry (δ).

Assuming that the conditions $c_{\mu,ion} \gg c_{\mu,n}$ and $c_{\mu,ion} \gg c_{\mu,p}$ are still valid, the approximation $c_n^{\delta} \approx c_{\mu,n}$ and $c_p^{\delta} \approx c_{\mu,p}$, as well as $v_e \approx v_{ion}$ can be used. This treatment accounts for the mixed conducting properties of the active layer and for the fact that mobile ions are assumed to be majority carriers (MC-i approximated model). Such a simplification, for the case of a solar cell with selective contacts and fast electronic transport, is displayed in Fig. 5.

While separating the total current into an ionic-electrostatic component and an electronic component is
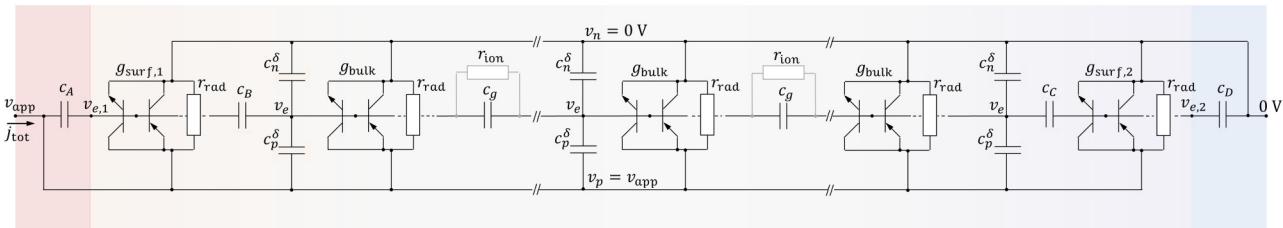

FIG. 5. Mixed conductor with mobile ionic majority carriers approximation (MC-i) for a solar cell with ideal selective and ion-blocking contacts. The model can account for the effect of large electronic charge concentrations via the chemical capacitors c_n^{δ} and c_p^{δ}. The circuit is obtained from Fig. 2(a), with the approximation $v_e \approx v_{ion}$ in the bulk (valid for angular frequencies $\omega > 0$), fast electronic transport, and by introducing the space-charge capacitors c_B and c_C in the active layer, as discussed for Fig. 4(b).

no longer possible, a reasonably simple expression of $v_e(x, \omega)/v_{\text{app}}$ that also accounts for electronic contribution to the electrostatic potential through the c_n^δ and c_p^δ terms is obtained [Eq. (C8)]. Equation (C13) yields the overall impedance $Z(\omega)$ of the circuit (MC-i approximation). Its expression reduces to the results obtained for Fig. 4 for the low electronic charge concentration case (IC solution). Note that the $\hat{c}$ element is no longer needed in the circuit, as approximations for the electronic capacitive contributions are explicitly considered in Fig. 5 through c_n^δ and c_p^δ. The approach used to obtain the MC-i circuit can be generalized to treat situations where the chemical capacitance associated with any one charge carrier (ionic or electronic) is dominant (e.g., MC-n: $L_{D,n} \ll L$, $L_{D,n} \ll L_{D,\text{ion}}$ and $L_{D,n} \ll L_{D,p}$).

In Fig. 5, the changes in electrostatic potential in the active layer are dictated not only by the ionic charging of interfacial capacitors, as seen in the IC approximation scenario, but also by the ionic and electronic charging of bulk chemical capacitors. The latter process is associated with the ambipolar diffusion of electronic and ionic charges (chemical diffusion of the neutral component), which leads to stoichiometric polarization effects in the bulk. While mostly established for mixed conducting devices in the dark under local equilibrium [42,51–53], stoichiometric polarization effects have been discussed also in the context of oxide-based high-temperature photoelectrochemical devices under illumination [54,55].

The characteristic time constant of this bulk diffusion process, τ^δ, is associated with the product of a chemical resistance r^δ and a chemical capacitance c^δ. In Fig. 5, these correspond to $r_{\text{ion,bulk}}$ (assuming negligible electronic transport resistance) and to $c_n^\delta + c_p^\delta$ integrated over the bulk of the active layer, respectively [56]. For the case of stoichiometric polarization close to equilibrium, a proportionality prefactor of 1/12 is needed in the calculation of the low frequency time constant, due to the evolution of the potential profile during the polarization process [2]. Here, such a prefactor is expected to depend on the specific device and steady-state situation considered. Note that, if the impedance associated with electronic transport cannot be neglected, the r_j and $g_{\mu,j}$ terms ($j = n, p$) as well as the recombination elements, are also involved in the determination of τ^δ.

Of note, the time constant τ^δ scales with the concentration of electronic charges (included in the chemical capacitance terms), and with the active-layer thickness squared [2,31]. It follows that τ^δ is very short in thin-film mixed conducting solar cells with low electronic charge concentrations. Because of that, and since the electronic contribution to the electrostatics is negligible, stoichiometric polarization effects are not visible in the electrical response for low bias and intrinsic active layers. Under large bias, the values of c_n^δ and/or c_p^δ (and therefore τ^δ) increase. If $L_{D,p} < L$ and/or $L_{D,n} < L$, the

ambipolar diffusion dynamics (charging of the chemical capacitors) gives rise to significant changes in v_e. This modulates recombination voltage driving forces and the corresponding currents, introducing an additional low-frequency feature in the impedance spectrum (see the next section).

Besides τ^δ, also $\tau^\perp$ is expected to change with the bias condition. Particularly in situations where the value of $c^\perp$ is limited by the presence of a depletion interfacial capacitor in the device, its dependence on bias is expected to be milder than for c^δ. The relation $\tau^\perp > \tau^\delta$ is then valid only for low enough c^δ (intrinsic active layer under low bias and thin films). Due to the charging of c_n^δ and c_p^δ occurring also during the space-charge polarization process, these elements contribute to the determination of the low-frequency time constant in the MC-i approximation (Appendix C). Such a contribution is negligible only if the value of c^δ integrated along the device thickness is significantly lower than the interfacial capacitance terms. It follows that τ^δ and $\tau^\perp$, as defined above, and the low-frequency impedance characteristic times depend on the properties of the active layer and of the contacts (including their selectivity), as well as on the applied bias.

D. Interpretation and discussion of calculated impedance spectra

The impedance of devices at equilibrium or under bias at steady state can be calculated using the equivalent circuit models presented in the previous sections. In this section, solar cells with a mixed conducting active layer and ion-blocking contacts are considered, with input parameters that are relevant to halide perovskite devices (see Secs. V, S10, and S11 in the Supplemental Material [39]). First, the proposed complete model is validated based on the comparison with drift-diffusion simulations. A situation where recombination integrated across the active-layer bulk is slightly larger than the recombination occurring at the interfaces is considered (Fig. 6, input parameters shown in Table S3 within the Supplemental Material [39]). The analysis of this general situation validates the model in its one-dimensional form (additional examples for cases with electronic transport limitations are shown in Figs. S24 and S25 within the Supplemental Material [39]). In the second part of this section, the influence of bias condition and recombination properties of solar cells on the calculated impedance is studied by applying the IC and MC-i approximations to specific examples (Fig. 7).

In Figs. 6(a) and 6(b), Bode plots show the calculated impedance of a solar cell with a mixed conducting active layer under open-circuit conditions in the dark and for different steady-state bias light intensities. The impedance obtained from drift-diffusion simulations using the method described in Refs. [13,48] is compared with the impedance calculated using the complete model (Fig.
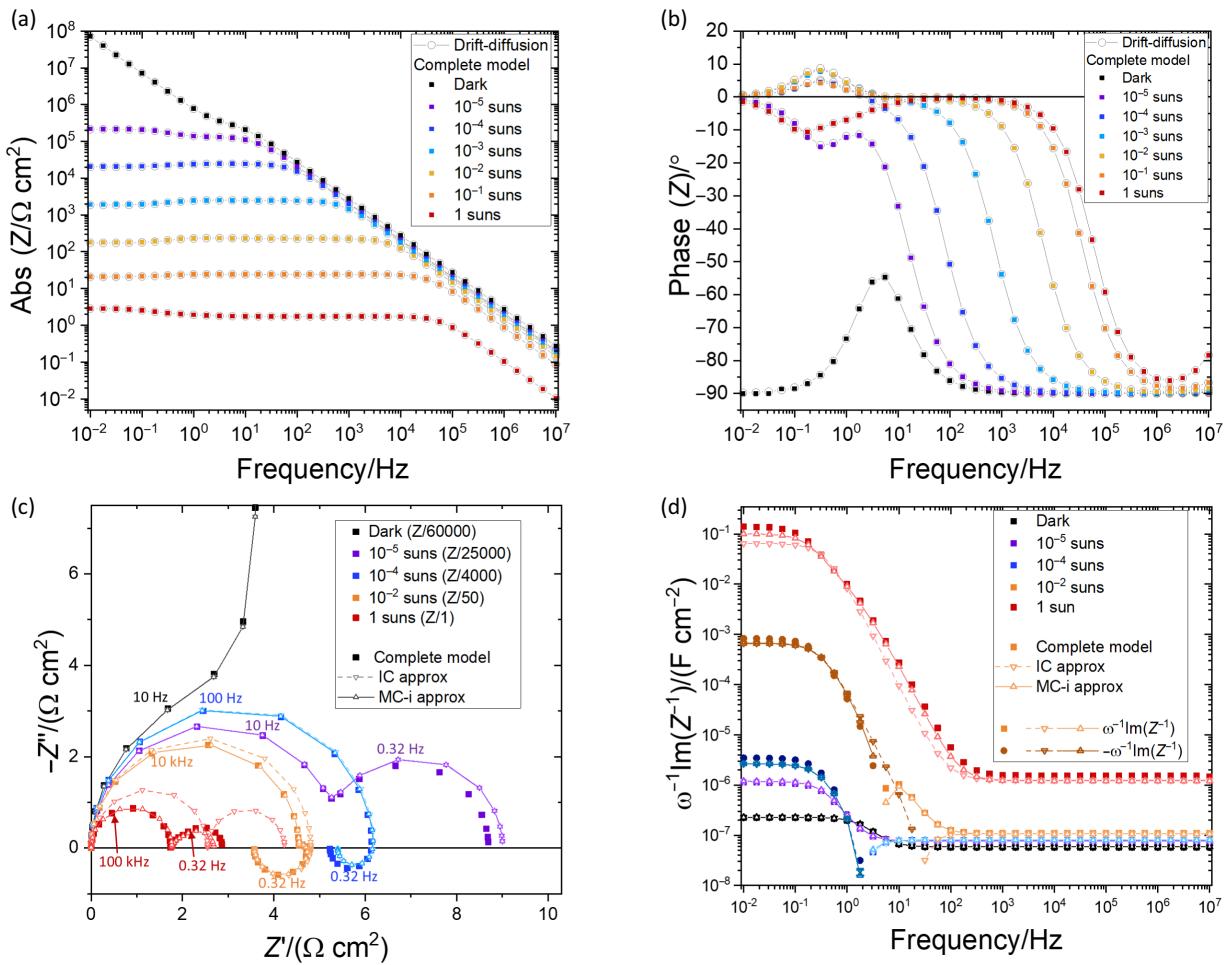
FIG. 6. Impedance of a solar cell based on a semiconducting active layer with mobile ions calculated using either drift diffusion or the transmission-line transistor-based equivalent circuit models presented in this study. Bode plots of the (a) magnitude and (b) phase of the impedance evaluated at open circuit in the dark and for different bias light intensities. The data obtained using the equivalent circuit model in Fig. S3 within the Supplemental Material [39] (complete model) are compared with drift-diffusion simulation results. (c),(d) show the Nyquist and apparent capacitance-frequency spectra of selected data from (a),(b), where the results obtained with the complete transmission line and the approximated IC and MC-i models are compared.

S3 within the Supplemental Material [39]). Both calculated results refer to the same steady-state drift-diffusion solutions. The datasets obtained with the two different methods match with good accuracy, confirming the analytical correspondence of the proposed equivalent circuit model with the linearized drift-diffusion equations.

The selected example highlights various transitions in the low-frequency impedance as a function of bias, as shown in the Nyquist plot and apparent capacitance-frequency spectra in Figs. 6(c) and 6(d). These data emphasize several of the key factors determining the small-perturbation electrical response of the device, including the following:

(1) Ionic-to-electronic current amplification effects at the interfaces and in the bulk, giving rise to one or two low-frequency impedance features associated with either capacitive or inductive behavior.

(2) The contribution of ionic conduction to the impedance at low electronic charge concentrations.

(3) Transition from impedance spectra that can be explained with the IC approximation (data for dark, 10^{-5} and 10^{-4} suns bias) to situations where the MC-i approximation is more appropriate (10^{-2} suns and 1 sun data). This transition is evident from the emergence of a second low-frequency feature, and it occurs at bias conditions leading to enhanced high-frequency capacitance due to electronic contribution in the active layer [Fig. 6(d)].

(4) Changes in shape of the low-frequency features at different bias due to changes in the relative magnitude of the steady-state concentration of electrons and holes in the bulk (see 10^{-2} suns vs 1 sun data).

(5) Effect of the magnitude of $\bar{V}_{app}$ relative to ϕ_{bi} and inversion in the majority carrier type at interfaces (relevant to situations where surface recombination dominates, this is not the case in Fig. 6).
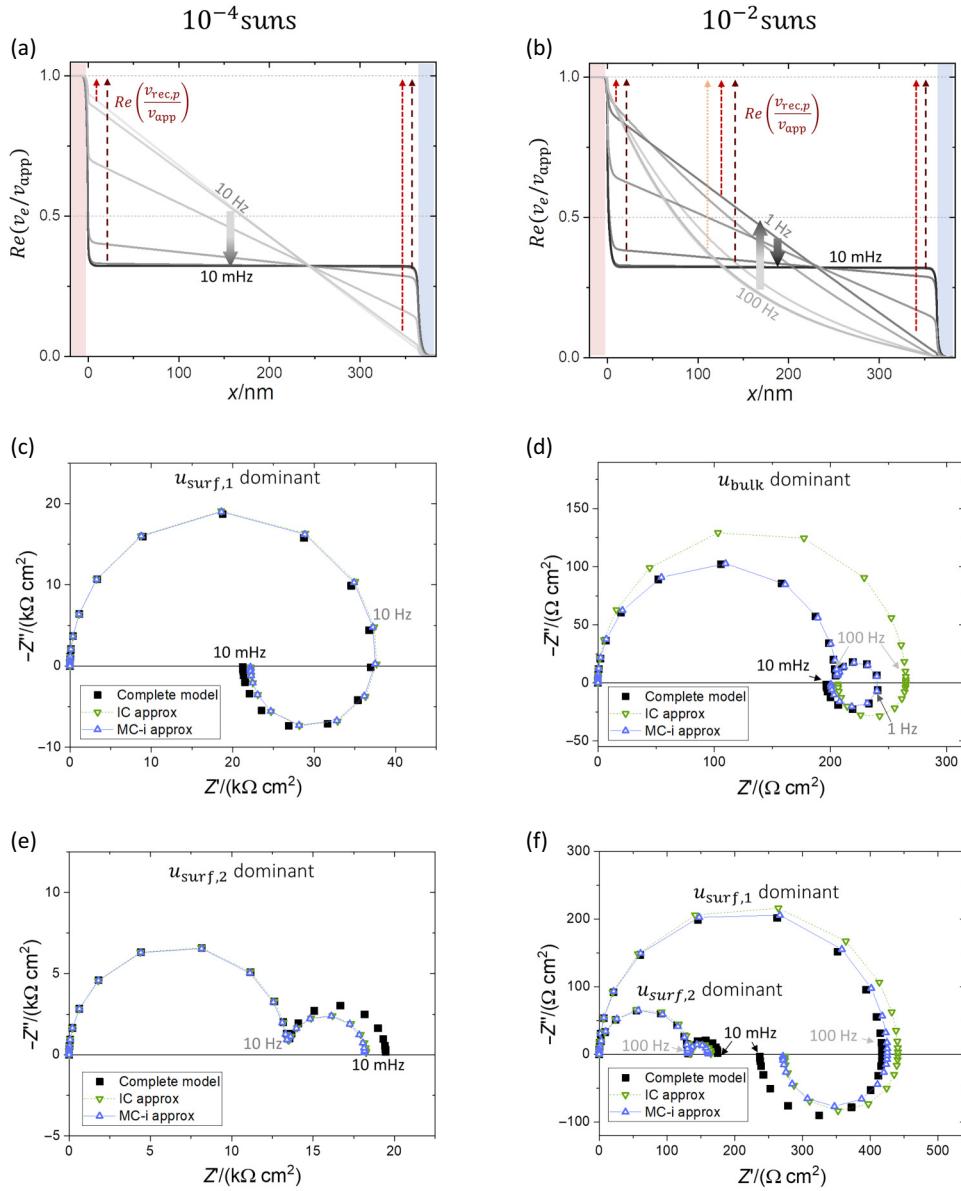
FIG. 7. Impedance of mixed conducting solar cells under bias at open circuit explained based on the frequency-dependent profile of the small-signal electrostatic potential v_e. The left column and the right column refer to light intensities of 10^{-4} and 10^{-2} suns, respectively. (a),(b) show the real part of the v_e/v_{app} function extracted from the solution of the complete model as a function of position in the device and for different frequencies. (c)–(f) Nyquist plot showing the impedance calculated with either the complete model based on the drift-diffusion steady-state solution, or with the IC or MC-i approximated circuit models (see Sec. V for details). The same input parameters are used to obtain the steady-state condition in all cases (see Sec. S11 within the Supplemental Material [39]), except the carrier capture lifetimes in the active layer and at interfaces 1 and 2. Specifically, $\tau_n = \tau_p$ in each region, and their value is varied to select situations where the recombination current at either interface 1 or 2, or in the bulk is dominant. Data in (a) and in (b) refer to the input parameters used for calculations shown in (c),(d), respectively.

Further discussion of these factors with reference to the data in Fig. 6, as well as of the influence of electronic transport limitations, is reported in Sec. S12 within the Supplemental Material [39].

Figure 7 shows additional representative cases, with a focus on the significance and validity of the IC and MC-i approximated models. The discussion presented below emphasizes that, for the case of mixed-conducting solar cells with efficient electronic transport, impedance spectra are largely dictated by the frequency dependence of the recombination current. As a result, impedance features can be interpreted based on two factors [see also Eq. (16)]. The first factor is the evolution of v_e with frequency in the region of the device hosting the dominant recombination

current. Such a region can be localized at surface 1, at surface 2, or can extend throughout the bulk of the active layer. The second factor is the magnitude of the relevant (trans)conductance terms $g_{rec,k}$.

To highlight this message, the capture lifetime of electrons and holes at the interfaces and in the bulk are varied to access different responses in Figs. 7(c)–7(f) (all other input device parameters are the same). Here, $\tau_n = \tau_p$ is used, for simplicity. Section S2 within the Supplemental Material [39] discusses the influence of the relative magnitude of τ_n and τ_p on the type of the recombination limiting carrier, and therefore on the dominant transconductance and recombination current.

The v_e profiles obtained from the solution to the complete model allow the evaluation of the changes in recombination voltages. These are $v_{rec,n} = v_e - v_n \approx v_e$ and $v_{rec,p} = v_p - v_e \approx v_{app} - v_e$ for the *npn* and *pnp* transistors, respectively (assuming fast electronic transport). Because in all cases considered in Fig. 7 $g_{rec,p} \gg g_{rec,n}$ (holes are minority carriers), only $v_{rec,p}$ is highlighted in Figs. 7(a) and 7(b), with arrows indicating its normalized real part $Re(v_{rec,p}/v_{app})$ at specific positions and for different frequencies. Once again, the driving force for radiative recombination is independent of position and of the frequency of the applied perturbation for cases involving efficient electronic transport and ideal contacts with opposite selectivity ($v_{rec,rad} = v_p - v_n \approx v_{app}$).

The frequency-dependent $Re(v_e/v_{app})$ data for the 10^{-4} suns case highlight an essentially linear v_e profile within the bulk of the active layer, with its slope (electric field) varying from a finite value to approximately zero for decreasing frequency. This corresponds to the transition from the short-range dielectric response of the device stack to the response due to long-range ionic redistribution (space-charge polarization with time constant $\tau^\perp$) at high and low frequencies, respectively. Note that the value of v_e in the bulk at low frequency is lower than $v_{app}/2$ because of the asymmetry in the interfacial capacitors (in this case $c_B \approx c_C$ and $c_A < c_D$).

Figures 7(c) and 7(e) show the resulting impedance depending on whether the electronic charge carriers' lifetime is shortest at interface 1 or 2, respectively. In the former case, a negative capacitance (or inductive behavior) is observed, due to the increase in recombination voltage $v_{rec,p}$ (decrease in impedance) with decreasing frequencies at interface 1 [see Fig. 7(a)]. The opposite dependence of $v_{rec,p}$ is observed for interface 2, leading to a low-frequency feature with (positive) capacitive behavior when recombination at such an interface dominates. It can be concluded that recombination of the rate-limiting electronic carrier in proximity to the interface where either such carrier type or the opposite carrier type is injected leads to negative or positive capacitance behavior at low frequencies, respectively.

When performing the same analysis for the data associated with high light intensities (10^{-2} suns), an additional regime is found. A nonlinear $Re(v_e/v_{app})$ profile in the active layer [Fig. 7(b)] dictates the recombination driving forces and currents in the bulk and at interfaces at high frequencies (e.g., 100 Hz). This result can be assigned to the electronic charging of the chemical capacitors c_n^δ and c_p^δ, which occurs already at fast time scales. As discussed in the previous section, such an effect happens at any bias conditions, but only for situations involving large enough steady-state electronic charge concentrations it influences v_e significantly. In other words, when c_n^δ and/or c_p^δ cannot be neglected, the bulk of the device cannot be approximated as electroneutral at high frequencies. As a result, the capacitance observed at high frequencies is expected to deviate from the geometric contribution. Its value is attributed to the dominant electronic capacitance contribution. This can be an interfacial electronic capacitor or $c_{\mu,eon,tot}$, as mentioned in the previous section (see also Appendix B and Sec. S6.1 within the Supplemental Material [39] for detailed discussion). If transport of electrons and holes is sluggish, electronic charging of the active layer's bulk occurs only at frequencies that are lower than the rate of electronic transport (see discussion of Figs. S26–S31 within the Supplemental Material [39]).

Electroneutrality and a linear profile of $Re(v_e/v_{app})$ in the bulk are established only at frequencies that are low enough so that ionic charges can redistribute within the bulk. Once again, this polarization involves the ambipolar diffusion of ionic and electronic charges in the bulk of the active layer and occurs over time scales in the order of τ^δ. At even lower frequencies, the space-charge polarization (plus further stoichiometric polarization) described above occurs also in this case.

Figure 7(d) displays the implications of such evolution in v_e in terms of the impedance spectral shape, for the case where bulk recombination is dominant. The resulting impedance highlights two clear features at low frequencies, one related with the bulk diffusion process and one related with the space-charge polarization with characteristic frequencies of approximately $(2\pi\tau^\delta)^{-1}$ and approximately $(2\pi\tau^\perp)^{-1}$ (for $\tau^\delta \ll \tau^\perp$), respectively (see Eq. (C8) for the exact solution to the MC-i problem). In this specific example, the ambipolar diffusion process leads to a decrease in recombination driving force for decreasing frequencies and to an increase in impedance highlighted by a feature with positive capacitance occurring in the 100–1 Hz frequency range. The increase in $v_{rec,p}$ caused by space-charge polarization at even lower frequencies (1–0.01 Hz) leads to a negative capacitive feature.

Interestingly, when the dominant recombination contribution is at either interface of the device, only one low-frequency feature (associated with space-charge polarization) is evident [Fig. 7(f)], even at large bias conditions.

This is consistent with the minimal variation in electrostatic potential (and in $v_{\text{rec},p}$) at the interfaces during the bulk polarization occurring in the 1–100 Hz frequency range [see Fig. 7(b)].

For cases where both polarization processes are visible in the impedance spectrum, two features with two positive, two negative, or one positive and one negative capacitive behavior are possible. Figures S16–S20 within the Supplemental Material [39] show that, whether the minority or the majority electronic charge carrier is limiting recombination in the bulk determines the nature of the intermediate frequency feature associated with stoichiometric polarization (positive or negative capacitive behavior, respectively) [29]. The discussion in Secs. S12.2 within the Supplemental Material [39] emphasizes that a more complex picture describes the situation where electronic transport is limiting the device current and the overall impedance of the device. Gating of charge-transport current (due to the j_μ elements) by the changes in the charge-carrier chemical potential can lead to "transport limited" low-frequency impedance features. Of note, because such a gating effect is sensitive to the local v_e in the region that is rate limiting to charge transport, it is not necessarily confined to the position hosting the dominant recombination process in the device (e.g., the presence of two low-frequency feature does not imply dominant bulk recombination).

Figures 7(c)–7(f) [as well as Figs. 6(c) and 6(d)] compare the impedance data obtained with the complete model with the IC and MC-i approximated models described above. While for the low electronic charge concentration case the IC and MC-i models essentially coincide and well describe the device response, at large bias only the MC-i model returns a satisfactory spectral shape. Interestingly, if c_n^δ and c_p^δ integrated across the bulk are small compared with the interfacial capacitors, then the IC model can reproduce the low-frequency feature associated with space-charge polarization (time constant approximately $\tau^\perp$), despite the presence of the ambipolar diffusion feature [e.g., 10^{-2} suns data in Figs. 6(c) and S16 within the Supplemental Material [39]]. If, however, c_n^δ and/or c_p^δ contribute significantly also to the low-frequency polarization process, such correspondence is no longer there (e.g., 1 sun data in Fig. 6(c), 10^{-2} suns data in Figs. 7(d), and S17–S20 within the Supplemental Material [39]). Therefore, even though including the $\hat{c}$ element in the IC approximation allows for an acceptable description of the capacitive behavior at high frequencies [see Fig. 6(d)], the influence of c_n^δ and c_p^δ on the magnitude and frequency dependence of the v_e profile at low frequencies can only be captured with the MC-i approximation (see Appendix C). Some discrepancies in the dataset obtained with the complete and the approximated models are present [e.g., low-frequency impedance in Figs. 7(e) and 7(f)] and are expected to be due to the method used to estimate the recombination voltage at the interfaces (see Sec. V).

The equivalent circuit modeling approach presented in this work facilitates the study of devices for which electron-hole recombination processes play an important role in the electrical response. The analysis emphasizes that the frequency dependence of the driving force associated with the dominant recombination process largely determines the impedance of the device at low frequencies. In the context of halide perovskite solar cells, this also means that mobile ions can be an unlikely researcher's "ally" when investigating the nature of such a dominant recombination process.

The transistor-based treatment of recombination integrated within a transmission line model may provide a more general physical interpretation of solar-cell behavior, including the discussion of parameters such as the device's ideality factor, and the analysis of other time- and frequency-domain measurements. Relating such information to physical properties (e.g., ϕ_{bi}, L_D, charge carrier concentrations, recombination lifetimes) should be subject of future studies. Finally, the model can be extended to account for other aspects [e.g., multiple mobile ionic species, nonideal contacts, redox reactions, explicit treatment of traps and of (de)trapping processes], extending its relevance to a broad range of photoelectrochemical devices.

IV. CONCLUSIONS

Linearization of the radiative and nonradiative recombination rates in semiconductors reveals that resistors and transistors, respectively, are the accurate equivalent circuit elements representing these processes in the small-perturbation regime. Integrating such elements in a transmission line results in a circuit that is analytically equivalent to the linearized drift-diffusion model. The equivalent circuit model emphasizes the dependence of recombination on the local changes in electrostatic potential, a general effect relevant to semiconducting materials with or without mobile ions. Such an influence can be ignored in most cases involving semiconductors with negligible mobile ionic concentrations, leading to an approximated description of recombination through simple resistor elements. On the other hand, in the presence of large mobile ion concentrations, as is the case in halide perovskite solar cells, the influence of ion redistribution on the electrostatic potential results in frequency-dependent recombination currents that largely dictates the electronic response of the device at low frequencies. The analysis of ionic-to-electronic current amplification effects occurring at interfaces [13] is extended to the bulk recombination and for situations where the electronic charge also influences the electrostatic potential. The discussion of stoichiometric polarization effects, in addition to the well-established space-charge polarization, occurring in mixed conducting devices is addressed for the nonequilibrium

case. Simplified analytical solutions for the overall device impedance in selected application relevant situations are derived and can aid the analysis and fitting of experimental data. The method and models proposed in this work provide a general platform for the study of the electrical response of semiconducting and mixed ionic-electronic conducting devices under light and/or voltage bias.

V. METHODS

A. Drift diffusion and complete equivalent circuit model calculations

Impedance calculations performed using drift-diffusion simulations are based on the method described in Refs. [13, 48], using the Driftfusion software [57]. The impedance calculations of all equivalent circuit models described in this work are performed using MATLAB codes that include the system of equations associated with Kirchhoff's current law at all nodes minus one (see Secs. 10 and 15 within the Supplemental Material [39]). Data presented in the main text involve calculations in the frequency range 10 MHz–10 mHz, with four data points per decade, performed assuming devices at room temperature. For the determination of the values of the equivalent circuit elements in the discretized model, information on the steady-state situation is needed. For the data obtained using the complete model (Figs. 6 and 7), the steady-state solution is obtained from the Driftfusion software. The same approach is expected to apply to other simulation tools that can provide the position-dependent charge concentrations and electrostatic potential. The circuit model shown in Fig. S3 within the Supplemental Material [39] is used, where the transmission line is extended to the contact layers. This accounts for generation and recombination processes occurring in contacts 1 and 2 (for calculations relevant to solar cells, these are referred to as the hole-transport material, HTM, and the electron-transport material, ETM, respectively), as well as for nonideal contact selectivity. The elements are defined on a mesh that includes the position of the voltage nodes $x_{i+1/2}$ ($i = 1, 2, \ldots N$) and the position associated with the elements connecting neighboring voltage nodes x_i ($i = 1, 2, \ldots N + 1$) (see Sec. S13 within the Supplemental Material for details on the discretized model [39]). Below, the method to evaluate the equivalent circuit elements is described, following previously reported analysis [7,41].

To model *charge transport* of charge carrier j, the relation describing the total (particle) current density as a function of the carrier concentration and mobility (n_j and u_j, respectively) and the gradient of the relevant electrochemical potential is considered:

$$J_j = -qu_j n_j \frac{dV_j}{dx}. \tag{24}$$

The relation is valid for electronic charges and monovalent ions. Differentiation of Eq. (24) yields

$$j_j = -qu_j \left[\tilde{n}_j \frac{d\bar{V}_j}{dx} + \bar{n}_j \frac{\widetilde{dV_j}}{dx} \right]. \tag{25}$$

Since

$$\frac{\widetilde{dV_j}}{dx} = \frac{dv_j}{dx}$$

and, in the small-signal regime,

$$\tilde{n}_j \approx \bar{n}_j \frac{v_{\mu,j}}{V_{\text{th}}},$$

Eq. (25) can be expressed as

$$j_j = \frac{\bar{J}_j}{V_{\text{th}}} v_{\mu,j} - \sigma_j \frac{dv_j}{dx}. \tag{26}$$

The second term in Eq. (26) describes the small-signal particle current due to the steady-state local partial conductivity $\sigma_j = qu_j \bar{n}_j$, and the change in electrochemical potential gradient, dv_j/dx. This current component corresponds, in discretized form, to the current flowing through an electrochemical resistor defined at position x_i, $r_{i,j} = \Delta x_{i+1/2}/\sigma_{i,j}$, connected between the voltage nodes $x_{i-1/2}$ and $x_{i+1/2}$ ($\Delta x_{i+1/2} = x_{i+1/2} - x_{i-1/2}$). The first term in Eq. (26) describes the small-signal particle current density due to changes in chemical potential of carrier j. By defining the transport transconductance $g_{\mu,j} = \bar{J}_j/V_{\text{th}}$, such current component can be expressed as $j_{\mu,j} = g_{\mu,j} v_{\mu,j}$. In the discretized model of Fig. 2(a), $j_{\mu,j}$ is implemented as a voltage-controlled current source. Note that a controlled source is required here, because $j_{\mu,j}$ flows in the charge-carrier rail but it is proportional to $v_{\mu,j}$, which is the potential difference between nodes of such a rail and of the electrostatic rail. Evaluation of $j_{\mu,j}$ flowing from node $x_{i-1/2}$ to $x_{i+1/2}$ requires calculating the average of $v_{\mu,j}$ at these two positions. For this reason, two current sources are used to represent this current component at each interval in Ref. [41]. In this work, a single current source controlled by the average of $v_{\mu,j}$ at position $x_{i-1/2}$ and $x_{i+1/2}$ is used at each x_i position for simplicity.

To model *charge storage*, the local chemical capacitance per unit volume associated with charge carrier j is defined as $c'_{\mu,n_j} = q\tilde{n}_j/v_{\mu,j}$. In the absence of significant trapping and assuming a dilute defect situation, the discretized chemical capacitance associated with node $x_{i+1/2}$ can be expressed as

$$c_{i+1/2,\mu,n_j} = \Delta x_i \frac{q\bar{n}_j}{V_{\text{th}}}, \tag{27}$$

where $\Delta x_i = x_{i+1} - x_i$.

Finally, the *electrostatic capacitors* are defined based on the local geometric capacitance as

$$c_{i,g} = \frac{\epsilon_i}{\Delta x_{i+1/2}}, \tag{28}$$

where ϵ_i is the local dielectric constant.

B. Approximated equivalent circuit models

The equivalent circuit elements used in calculations involving the IC and MC-i approximated models in Figs. 4 and 5 are evaluated based on the steady-state solution described above. For the bulk parameters (e.g., $r_{\text{ion,bulk}}, g_{\text{rec,bulk}}, c_n^\delta$ and c_p^δ), a single value is used and estimated by considering the charge concentrations in the middle of the active layer. This approximation represents a source of error in the impedance calculation, as the transconductance profiles vary especially within the space-charge regions in the active layer with possible local maxima (e.g., in general $\bar{p} \neq \bar{n}$ in the bulk, while the condition $\bar{p} = \bar{n}$, and therefore large values of g_{rec}, can occur in a localized region of the space charges). For the interfacial parameters, values of recombination transconductance are obtained by integrating their value over the junction layers (in this case 2 nm in thickness) used in the Driftfusion software to describe the interfaces [57]. Interfacial capacitors c_A, c_B, c_C, and c_D are defined based on the steady-state concentration of the majority carrier in the relevant layer's bulk and on the space-charge potential [27,58]. For example, the space-charge capacitance associated with contact 1 (HTM for the case of a solar cell) is evaluated based on

$$c_A = \text{sign}(\bar{\phi}_A)\sqrt{\frac{q\epsilon_{\text{HTM}}N_A}{2V_{\text{th}}}}\frac{1 - e^{-(\bar{\phi}_A/V_{\text{th}})}}{\sqrt{e^{-(\bar{\phi}_A/V_{\text{th}})} + (\bar{\phi}_A/V_{\text{th}}) - 1}}, \tag{29}$$

where ϵ_{HTM} and N_A are the dielectric constant and the acceptor doping density in the HTM (the latter is assumed to correspond to the hole concentration in the contact's bulk). Equation (29) can be used to evaluate the other interfacial capacitors too, by replacing the relevant space-charge potential, dielectric constant, and bulk majority carrier concentration (e.g., p in the HTM, n_{ion} in the active layer, and n in the ETM, for the mixed conducting solar cells in this work). Note that $\bar{\phi}_A$ is defined to be positive for space-charge situations leading to depletion of majority carriers in the HTM. For the calculation of c_B, the relevant space-charge potential should be included in Eq. (29) with a negative sign, as depletion of the positive ionic species occurs for negative values of $\bar{\phi}_B$, as defined in Fig. 2(b). Because significant changes in the steady-state electrostatic potential occur within the junction layers used in the drift-diffusion simulations, the use of a single estimate for each space-charge potential in the

calculation of the interfacial capacitors can be a source of discrepancy between the approximated and the complete models. In this study, the space-charge potentials are calculated considering the potential in each of the layers' bulk and the potential at the outer boundary of the junction layer (interface between each junction and the respective contact layer). This approach is valid for negligible steady-state electric field values in the bulk of the active layer, as is expected for the IC and MC-i approximations.
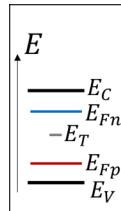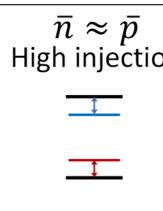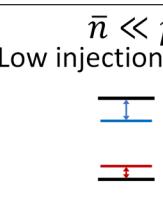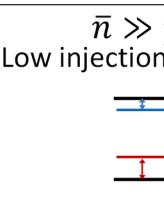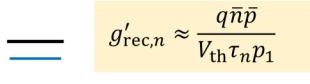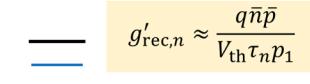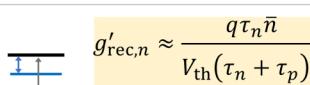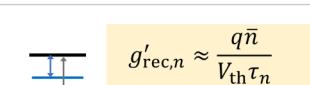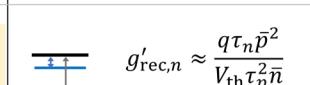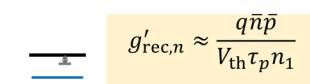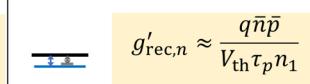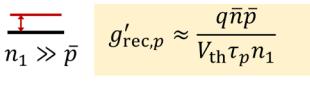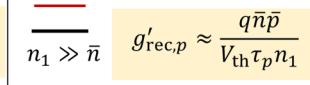
APPENDIX A: STEADY-STATE ELECTRONIC CHARGE CONCENTRATION AND RECOMBINATION TRANSCONDUCTANCE TERMS

Table I provides the approximated expression of the recombination transconductance parameters for the different possible situations relevant to the trap-mediated SRH recombination in a semiconductor, where light and/or electrical bias leads to QFLS > 0. These include situations where the steady-state concentrations of electrons and holes are comparable ($\bar{n} \approx \bar{p}$), commonly referred to as "high injection" in semiconductor physics, or where the two carriers differ significantly in concentration (where $\bar{n} \gg \bar{p}$ or $\bar{n} \ll \bar{p}$), referred to as "low injection." Note that the high- and low-injection terminology may be misleading in the case of mixed conductors, where the condition $\bar{p} \neq \bar{n}$ holds for most situations, even for devices under large bias (Sec. S8 within the Supplemental Material [39]). The analysis in Table I is carried out for the cases where either a shallow or a deep trap is at play. Here, a trap is defined as shallow or deep depending on the relative position of the trap energy and of the electronic majority carrier(s) quasi-Fermi-level. That is, if either n_1 or p_1 is greater than both n and p, the trap is shallow and it is deep otherwise (the trap energy can be deep and yet not be between the quasi-Fermi-levels). In the table, the recombination transconductance terms that are expected to dominate the expression of u_{SRH} for each situation are highlighted. Similar values of τ_n and τ_p are assumed in the approximations shown in Table I, while different expressions are obtained based on Eq. (11) if these parameters are very different from each other, also affecting the dominant transconductance term. This point is discussed in Sec. S2 within the Supplemental Material [39], where the expressions for the generation transconductance terms are also shown (these have negligible contribution under light and/or forward voltage bias).

TABLE I. Expressions for the recombination transconductance terms describing SRH recombination in a semiconductor under light and/or electrical bias. Situations involving similar ($\bar{n} \approx \bar{p}$) or very different ($\bar{n} \ll \bar{p}$ or $\bar{n} \gg \bar{p}$) electronic charge concentrations are discussed (referred to as high- or low-injection, respectively, see text) for the deep or the shallow trap cases. All g'_{rec} terms have the units of A V^{-1} cm^{-3}. These simplified expressions are valid only if τ_n and τ_p have comparable values. Under such conditions, and assuming forward bias (or light bias) leading to QFLS > 0, dominant term(s) for each condition are highlighted in yellow. The energy-level diagram shows the position of the quasi-Fermi-levels (E_{Fn} and E_{Fp}) and of the trap energy (E_T) with respect to the conduction and valence-band edges (E_C and E_V).

| E	$\bar{n} \approx \bar{p}$ High injection		$\bar{n} \ll \bar{p}$ Low injection (p type)		$\bar{n} \gg \bar{p}$ Low injection (n type)	
Shallow trap (E_T close to E_V)	$g'_{\text{rec},n} \approx \dfrac{q\bar{n}\bar{p}}{V_{\text{th}}\tau_n p_1}$		$g'_{\text{rec},n} \approx \dfrac{q\bar{n}\bar{p}}{V_{\text{th}}\tau_n p_1}$		$g'_{\text{rec},n} \approx \dfrac{q\bar{n}\bar{p}}{V_{\text{th}}\tau_n p_1}$	
	$p_1 \gg \bar{p}$	$g'_{\text{rec},p} \approx \dfrac{q\bar{n}\bar{p}}{V_{\text{th}}\tau_n p_1}$	$p_1 \gg \bar{p}$	$g'_{\text{rec},p} \approx \dfrac{q\bar{n}\bar{p}}{V_{\text{th}}\tau_n p_1}$	$p_1 \gg \bar{n}$	$g'_{\text{rec},p} \approx \dfrac{q\bar{n}\bar{p}}{V_{\text{th}}\tau_n p_1}$
Deep trap	$g'_{\text{rec},n} \approx \dfrac{q\tau_n\bar{n}}{V_{\text{th}}(\tau_n+\tau_p)^2}$		$g'_{\text{rec},n} \approx \dfrac{q\bar{n}}{V_{\text{th}}\tau_n}$		$g'_{\text{rec},n} \approx \dfrac{q\tau_n\bar{p}^2}{V_{\text{th}}\tau_p^2\bar{n}}$	
	$p_1 \ll \bar{p}$ $n_1 \ll \bar{n}$	$g'_{\text{rec},p} \approx \dfrac{q\tau_p\bar{n}}{V_{\text{th}}(\tau_n+\tau_p)^2}$	$p_1 \ll \bar{p}$ $p_1 \ll \bar{n}$ $n_1 \ll \bar{n}$	$g'_{\text{rec},p} \approx \dfrac{q\tau_p\bar{n}^2}{V_{\text{th}}\tau_n^2\bar{p}}$	$p_1 \ll \bar{p}$ $n_1 \ll \bar{n}$ $n_1 \ll \bar{n}$	$g'_{\text{rec},p} \approx \dfrac{q\bar{p}}{V_{\text{th}}\tau_p}$
Shallow trap (E_T close to E_C)	$g'_{\text{rec},n} \approx \dfrac{q\bar{n}\bar{p}}{V_{\text{th}}\tau_p n_1}$		$g'_{\text{rec},n} \approx \dfrac{q\bar{n}\bar{p}}{V_{\text{th}}\tau_p n_1}$		$g'_{\text{rec},n} \approx \dfrac{q\bar{n}\bar{p}}{V_{\text{th}}\tau_p n_1}$	
	$n_1 \gg \bar{p}$	$g'_{\text{rec},p} \approx \dfrac{q\bar{n}\bar{p}}{V_{\text{th}}\tau_p n_1}$	$n_1 \gg \bar{p}$	$g'_{\text{rec},p} \approx \dfrac{q\bar{n}\bar{p}}{V_{\text{th}}\tau_p n_1}$	$n_1 \gg \bar{n}$	$g'_{\text{rec},p} \approx \dfrac{q\bar{n}\bar{p}}{V_{\text{th}}\tau_p n_1}$

As evident from Table I, for all cases involving a shallow trap, $g'_{\text{rec},n} = g'_{\text{rec},p}$ justifying the definition of a recombination resistance r_{SRH} according to Eq. (13) in the main text. For the case of deep traps, the terms $g'_{\text{rec},n}$ and $g'_{\text{rec},p}$ are in general different, implying that the complete transistor description is needed. When considering $\bar{n} \approx \bar{p}$ with a deep trap, $g'_{\text{rec},n}$ and $g'_{\text{rec},p}$ can be of similar magnitude. For the special case of $\tau_n\bar{p} = \tau_p\bar{n}$, one obtains $g'_{\text{rec},n} = g'_{\text{rec},p}$, and a recombination resistance $r'_{\text{SRH}} = 1/g'_{\text{rec}}$ can be adopted instead of the transistor model in this case, too. Table II summarizes these considerations.

APPENDIX B: EQUIVALENT CAPACITANCE AND IMPEDANCE APPROXIMATIONS FOR SOLAR CELLS WITHOUT MOBILE IONS

Figure 8 shows the capacitive transmission line associated with a semiconducting device with no mobile ions and ideal contacts with opposite electronic selectivity. By considering the differential value of the electrical elements $c'_\mu = dc_\mu/dx$, $c'_g = (d(c_g)^{-1}/dx)^{-1}$, the equivalent capacitance can be expressed as (see derivation in Sec. S6.1 within the Supplemental Material [39]):

$$c_{\text{eq}} = \{2c_A c_D c'_{\mu,n} c'_{\mu,p} + [c_A c_D(c'^{\,2}_{\mu,n} + c'^{\,2}_{\mu,p}) + c'_{\mu,n} c'_{\mu,p}(c_A + c_D)(c'_{\mu,n} + c'_{\mu,p})L]\cosh[\kappa L]$$
$$+ \kappa[c_A c'_{\mu,n}(c'_g c'_{\mu,n} + c_D c'_{\mu,p}L) + c'_g c'_{\mu,p}(c_D c'_{\mu,p} + c'_{\mu,n}(c'_{\mu,n} + c'_{\mu,p})L)]\sinh[\kappa L]\}$$
$$\times \{(c_A + c_D)(c'_{\mu,n} + c'_{\mu,p})^2 \cosh[\kappa L] + c'_g \kappa^3(c_A c_D + c'_g(c'_{\mu,n} + c'_{\mu,p}))\sinh[\kappa L]\}^{-1}, \tag{B1}$$

TABLE II. Expressions for the radiative and trap-mediated recombination terms for a semiconductor with QFLS > 0 under small-perturbation conditions, and their corresponding equivalent circuits. For the SRH transconductance, τ_n and τ_p are assumed to be of similar magnitude. If this is not the case, the full expression in Eq. (11) needs to be used.

Recombination term	Equivalent circuit
Radiative recombination $$qu_{\text{rad}} = \frac{v_p - v_n}{r'_{\text{rad}}}, \quad r'_{\text{rad}} = \frac{V_{\text{th}}}{qk_{\text{rad}}\bar{n}\bar{p}}$$	
SRH (deep trap, low injection, n type) $$qu_{\text{SRH}}(\bar{n} \gg \bar{p}) \approx g'_{\text{rec},p}(v_p - v_e), \quad g'_{\text{rec},p} = \frac{q\bar{p}}{V_{\text{th}}\tau_p}$$	
SRH (deep trap, low injection, p type) $$qu_{\text{SRH}}(\bar{p} \gg \bar{n}) \approx g'_{\text{rec},n}(v_e - v_n), \quad g'_{\text{rec},n} = \frac{q\bar{n}}{V_{\text{th}}\tau_p}$$	
SRH (deep trap, high injection) $$qu_{\text{SRH}}(\bar{n} \approx \bar{p}) \approx g'_{\text{rec},p}(v_p - v_e) + g'_{\text{rec},n}(v_e - v_n)$$ $$g'_{\text{rec},p} = \frac{q\bar{p}\tau_p}{V_{\text{th}}(\tau_n + \tau_p)^2}, \quad g'_{\text{rec},n} = \frac{q\bar{n}\tau_n}{V_{\text{th}}(\tau_n + \tau_p)^2}$$	
SRH (deep trap, $\tau_n\bar{p} \approx \tau_p\bar{n}$) $$qu_{\text{SRH}}(\tau_n\bar{p} \approx \tau_p\bar{n}) \approx \frac{v_p - v_n}{r'_{\text{SRH}}}, \quad r'_{\text{SRH}} = \frac{4V_{\text{th}}\tau_n}{q\bar{n}}$$	
SRH (shallow trap, e.g., E_T close to E_C) $$qu_{\text{SRH}}(n_1 \gg \bar{p}, \bar{n}) \approx \frac{v_p - v_n}{r'_{\text{SRH}}}, \quad r'_{\text{SRH}} = \frac{V_{\text{th}}\tau_p n_1}{q\bar{n}\bar{p}}$$	

where $\kappa = \sqrt{(c'_{\mu,p} + c'_{\mu,n})/c'_g}$.

The total impedance of the circuit in Fig. 3(a) can be obtained based on this result as

$$Z(\omega) = (r_{\text{rec,tot}}^{-1} + i\omega c_{\text{eq}})^{-1}. \tag{B2}$$

The modification to this problem to include situations that differ from the flat-band case and the discussion of the evaluation of c_{eq} in mixed conducting devices at high frequencies are presented in Sec. S6.1 within the Supplemental Material [39]. As discussed in the main text, an effective electronic capacitance can be expressed as $\hat{c} = c_{\text{eq}} - c_{g,\text{tot}}$ (parallel of $c_{g,\text{tot}}$ and $\hat{c}$ corresponds to c_{eq}).

APPENDIX C: IC AND MC-i APPROXIMATIONS TO THE TRANSMISSION-LINE PROBLEM

The complete differential problem associated with Fig. 2(a) has a complex solution, even when considering selective contacts and fast electronic transport (see
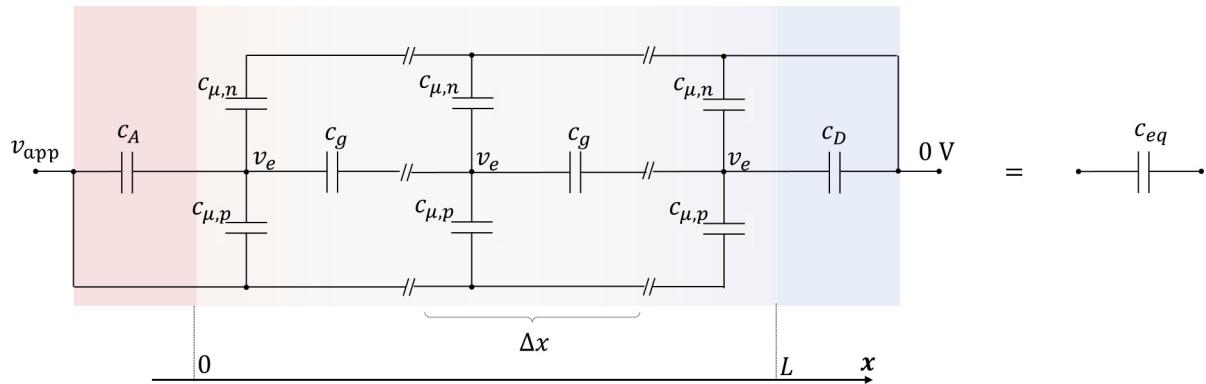
FIG. 8. Capacitive network associated with a semiconducting solar cell (no mobile ions) assuming selective contacts (with opposite selectivity) and fast transport ($r_{p,1}, r_{n,2}, r_p$, $r_n \approx 0$, and $r_{p,1}, r_{n,2} \to \infty$). The analytical expression of the equivalent capacitance c_{eq} depends on both the electrostatic and on chemical contributions (see text).

Sec. S6.2 within the Supplemental Material [39]). Simplified versions of the circuit model are considered here, for which more accessible analytical solutions are available.

Ionic conductor approximation (IC model)

Figure 9 shows the transmission-line circuit used for the determination of the small-signal electrostatic potential v_e in a mixed conducting device under the ion conductor approximation (IC model, Fig. 4). The circuit

essentially represents an ionic conductor between ion-blocking contacts (for a detailed discussion, see Sec. S6.3 within the Supplemental Material [39]). The widths of the space-charge widths at interfaces 1 and 2 on the active-layer side are indicated as λ_1^* and λ_2^*, respectively [Fig. 9(b)]. These correspond to the Debye length L_D in case of Gouy-Chapman situations (accumulation or small depletion of the majority carrier), while wider values may be expected for significant ionic depletion (Mott-Schottky situations). The model focuses on the changes in the values of ϕ_B and ϕ_C [see Fig. 2(c)], while it no longer explicitly describes the position dependence of v_e within the
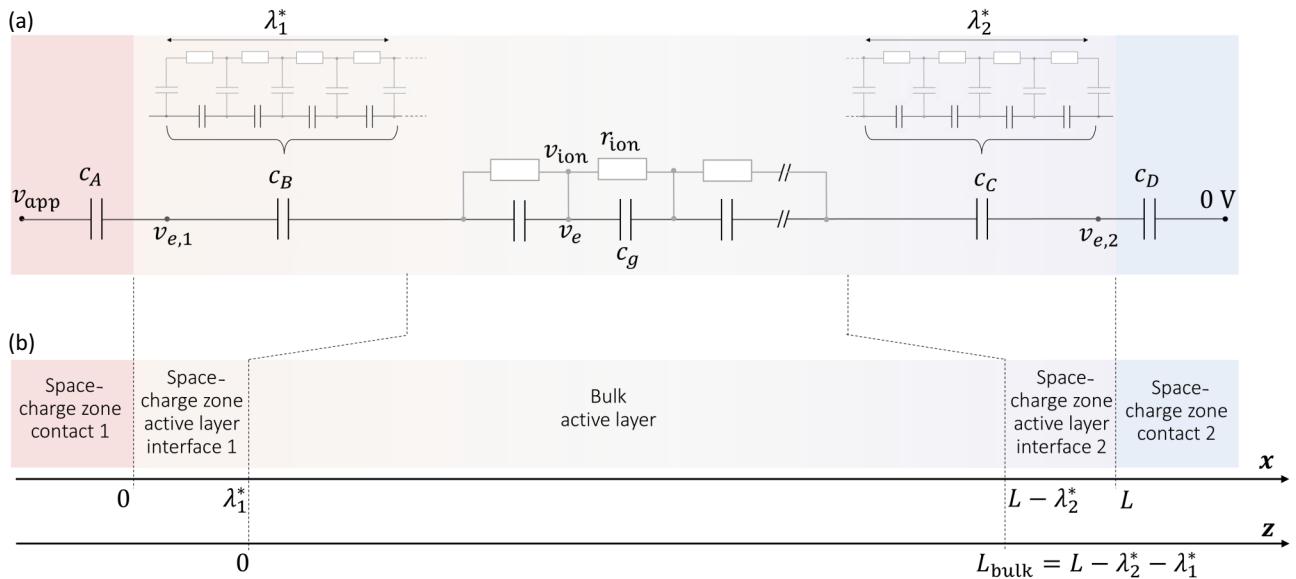

FIG. 9. (a) Approximated circuit determining the changes in electrostatic potential v_e in a mixed conducting device with ion-blocking contacts (IC approximation, see text). (b) Schematics of the full device highlighting the relation between the circuit elements in (a) and the different regions in the contacts and in the active layer. The space-charge widths in the active layer for interface 1 and interface 2 are indicated as λ_1^* and λ_2^*, respectively. The position variable z is introduced to describe the bulk of the device.

space-charge zones. Furthermore, because in the bulk $v_e \approx v_{\text{ion}}$ based on the assumption of large ionic chemical capacitance compared with the electronic counterparts, $c_{\mu,\text{ion}}$ elements can be replaced with short circuits, as shown in Figs. 4(b) and 9(a) (valid for nonzero angular frequencies, and only for the small perturbation analysis).

By defining a position variable describing the bulk as $z = x - \lambda_1^*$ and the bulk thickness as $L_{\text{bulk}} = L - \lambda_1^* - \lambda_2^*$, the solution $v_e(\omega, z)/v_{\text{app}}$ for $0 < z < L_{\text{bulk}}$ is obtained.

$$\frac{v_e(z, \omega)}{v_{\text{app}}} = \frac{c_1}{c_1 + c_2} \frac{1 + i\omega r_{\text{ion,bulk}}(c_{g,\text{bulk}} + (c_2 z/L_{\text{bulk}}))}{1 + i\omega r_{\text{ion,bulk}} c_1 c_2/(c_1 + c_2)}. \tag{C1}$$

Here $c_1 = \frac{c_A c_B}{c_A + c_B}, c_2 = \frac{c_C c_D}{c_C + c_D}, c_{g,\text{bulk}} = \frac{c'_g}{L_{\text{bulk}}},$ and $r_{\text{ion}} = L_{\text{bulk}} r'_{\text{ion}}$ (all differential parameters are assumed constant in the bulk).

The transfer function in Eq. (C1) provides the value of $v_e(x) = v_e(z + \lambda_1^*)$ for $0 < z < L_{\text{bulk}}$ given a (small) v_{app}. The value of $v_e(x)$ is also defined at the interfaces of the

active layer with the contacts as

$$v_{e,1}(\omega) = v_e(x = 0, \omega) = v_e(z = 0, \omega) \frac{c_B}{c_A + c_B}$$
$$+ v_{\text{app}} \frac{c_A}{c_A + c_B}, \tag{C2}$$

$$v_{e,2}(\omega) = v_e(x = L, \omega) = v_e(z = L_{\text{bulk}}, \omega) \frac{c_C}{c_D + c_C}. \tag{C3}$$

The impedance of the circuit in Fig. 9(a) can be expressed as

$$Z_{\text{ion},e}(\omega) = \frac{1}{i\omega c_1 c_2/(c_1 + c_2)} + \frac{r_{\text{ion,bulk}}}{1 + i\omega r_{\text{ion,bulk}} c_{g,\text{bulk}}}$$
$$= \frac{1 + i\omega r_{\text{ion,bulk}}(c_1 c_2/(c_1 + c_2) + c_{g,\text{bulk}})}{i\omega c_1 c_2/(c_1 + c_2)(1 + i\omega r_{\text{ion,bulk}} c_{g,\text{bulk}})}. \tag{C4}$$

By including the expressions for $v_e(\omega, z)/v_{\text{app}}$ [see Eq. (C1)] in Eq. (21) in the main text and the recombination contributions from the interfaces, one obtains the solution for the electronic impedance $Z_{\text{eon}}(\omega) = v_{\text{app}}/j_{\text{eon}}(\omega)$:

$$Z_{\text{eon}}(\omega) = \left\{ \frac{L}{r'_{\text{rad}}} + i\omega\hat{c} + \frac{v_{e,1}(\omega)}{v_{\text{app}}} g_{\text{rec},n,\text{surf1}} + \left(1 - \frac{v_{e,1}(\omega)}{v_{\text{app}}}\right) g_{\text{rec},p,\text{surf1}} + \frac{v_{e,2}(\omega)}{v_{\text{app}}} g_{\text{rec},n,\text{surf2}} \right.$$
$$\left. + \left(1 - \frac{v_{e,2}(\omega)}{v_{\text{app}}}\right) g_{\text{rec},p,\text{surf2}} + \int_0^{L_{\text{bulk}}} \left[\frac{v_e(z, \omega)}{v_{\text{app}}} g'_{\text{rec},n} + \left(1 - \frac{v_e(z, \omega)}{v_{\text{app}}}\right) g'_{\text{rec},p} \right] dz \right\}^{-1}, \tag{C5}$$

where the value of $\hat{c}$ can be evaluated using Eq. (B1). The overall impedance of the device is calculated using

$$Z(\omega) = [Z_{\text{ion},e}^{-1}(\omega) + Z_{\text{eon}}^{-1}(\omega)]^{-1}. \tag{C6}$$

In Figs. 4(c), 4(d), and 4(e) in the main text, further simplification to the model are shown, where the influence of the electrostatic potential on the bulk recombination is

not explicitly implemented. For these circuits, the total impedance can still be evaluated based on Eq. (C6), where

(1) Equation (C4) still allows the determination of $Z_{\text{ion},e}$.
(2) Equation (C5) is simplified to the following expression to yield an expression for Z_{eon}:

$$Z_{\text{eon}}(\omega) = \left\{ r_{\text{rec,bulk}}^{-1} + i\omega\hat{c} + \frac{v_{e,1}(\omega)}{v_{\text{app}}} g_{\text{rec},n,\text{surf1}} + \left(1 - \frac{v_{e,1}(\omega)}{v_{\text{app}}}\right) g_{\text{rec},p,\text{surf1}} + \frac{v_{e,2}(\omega)}{v_{\text{app}}} g_{\text{rec},n,\text{surf2}} + \left(1 - \frac{v_{e,2}(\omega)}{v_{\text{app}}}\right) g_{\text{rec},p,\text{surf2}} \right\}^{-1}. \tag{C7}$$

Mixed conductor with ionic majority carrier approximation (MC-i)

The MC-i approximation accounts for the fact that the electronic charge concentrations are large enough to influence the electrostatic landscape. Figure 10(a) shows the circuit network in Fig. 5, without the recombination elements. By solving the relevant differential problem coupled with boundary conditions (see Sec. S6.4 within the Supplemental Material [39]) one obtains

$$
\frac{v_e(\omega, z)}{v_{\mathrm{app}}} = \frac{c_p^{\delta'}}{c_p^{\delta'} + c_n^{\delta'}}
$$

$$
+ \frac{(1 - (c_2/c_1)(c_p^{\delta'}/c_n^{\delta'}))\cosh(\kappa z)(1 + i\omega r'_{\mathrm{ion}}c'_g)\kappa^2 + i\omega r'_{\mathrm{ion}}[(c_n^{\delta'} + c_p^{\delta'})(\cosh[\kappa(L_{\mathrm{bulk}} - z)] - \cosh[\kappa z]) + c_2\kappa(\sinh[\kappa(L_{\mathrm{bulk}} - z)] - (c_p^{\delta'}/c_n^{\delta'})\sinh[\kappa z])]}{(1 + (c_p^{\delta'}/c_n^{\delta'}))\{i\omega r'_{\mathrm{ion}}[(c_n^{\delta'} + c_p^{\delta'})(\cosh[\kappa L_{\mathrm{bulk}}] - 1) + c_2\kappa\sinh[\kappa L_{\mathrm{bulk}}]] + (1 + i\omega r'_{\mathrm{ion}}c'_g)\kappa^2(1 + (c_2/c_1)\cosh[\kappa L_{\mathrm{bulk}}] + ((c_n^{\delta'} + c_p^{\delta'})/\kappa c_1)\sinh[\kappa L_{\mathrm{bulk}}])\}},
$$

$$\tag{C8}$$

where the differential component chemical capacitors [e.g., $c_p^{\delta'} = dc_p^{\delta}/dx$] as well as the (frequency-dependent) parameter $\kappa = \kappa(\omega) = \sqrt{i\omega(c_p^{\delta'} + c_n^{\delta'})r'_{\mathrm{ion}}/(1 + i\omega r'_{\mathrm{ion}}c'_g)}$ are introduced.
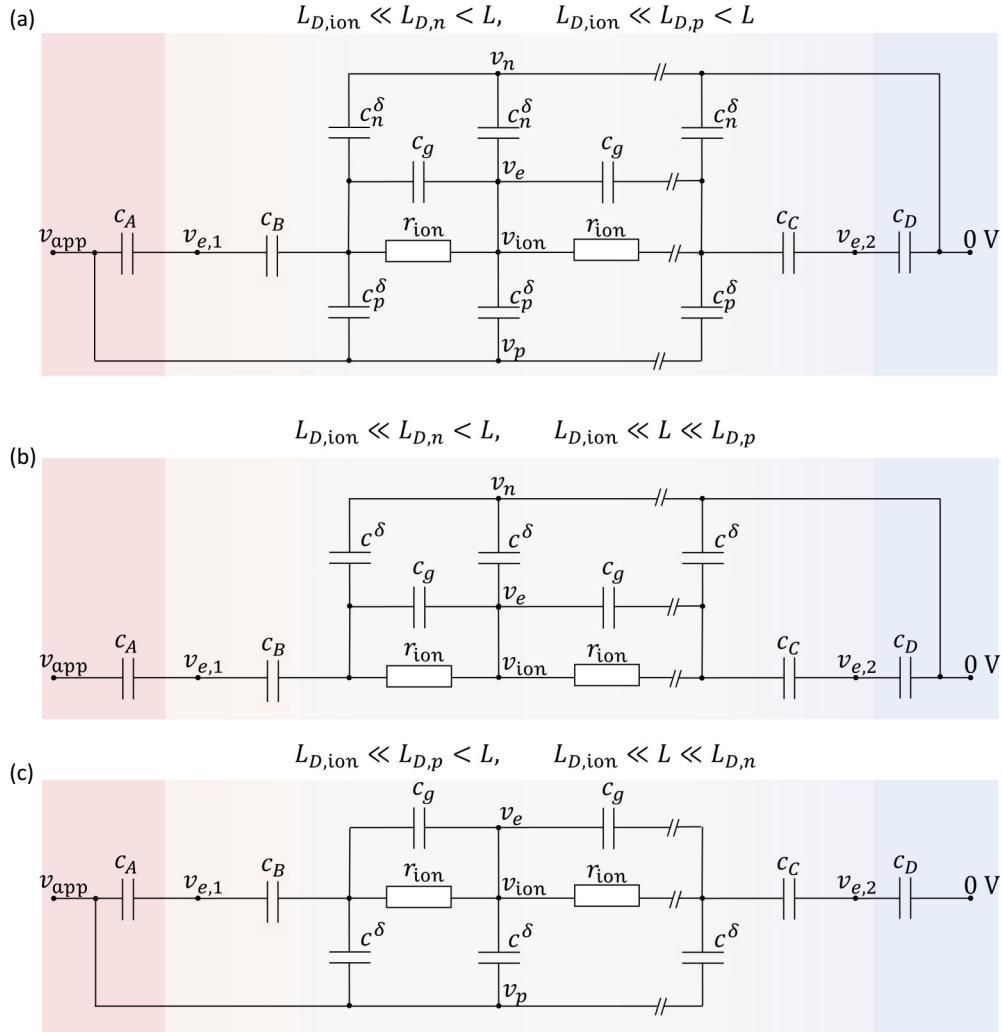

FIG. 10. (a) MC-i equivalent circuit model in Fig. 5, without the recombination circuit elements. (b),(c) show the simplified versions of (a) for situations where only (b) electrons or (c) holes influence significantly the electrostatic potential.

If only one of the two electronic charge carriers is present with large concentration, further simplification to the transmission lines can be applied. The resulting circuit considers only one type of chemical capacitors that involve mobile ionic defects and either electrons [Fig. 10(b)] or holes [Fig. 10(c)]. By defining $\kappa = \sqrt{i\omega c^{\delta'} r'_{\text{ion}}/(1 + i\omega r'_{\text{ion}} c'_g)}$, where $c^{\delta'} = c_n^{\delta'}$ or $c^{\delta'} = c_p^{\delta'}$, depending on the electronic majority carrier, slightly simpler solutions are obtained in these cases. For $\bar{p} \ll \bar{n}$ [Fig. 10(b)], one finds

$$\frac{v_e(\omega,z)}{v_{\text{app}}} = \frac{\cosh[\kappa(L_{\text{bulk}} - z)]}{\cosh(\kappa L_{\text{bulk}})}$$

$$\times \frac{1 + i\omega r'_{\text{ion}}\{c'_g + (c_2/\kappa)\tanh[\kappa(L_{\text{bulk}} - z)]\}}{(1 + (c_2/c_1)) + (c^{\delta'}/\kappa c_1)\tanh(\kappa L_{\text{bulk}}) + i\omega r'_{\text{ion}}[c'_g(1 + (c_2/c_1)) + ((c_2/\kappa) + (c^{\delta'} c'_g/\kappa c_1))\tanh(\kappa L_{\text{bulk}})]} \quad \text{(C9)}$$

$$\frac{v_e(z, \omega \to 0)}{v_{\text{app}}} \approx \frac{1}{1 + (c_2/c_1) + (c^{\delta'}/c_1)L_{\text{bulk}}} = \frac{c_1}{c_1 + c_2 + c^{\delta'}L_{\text{bulk}}}. \quad \text{(C10)}$$

For the $\bar{p} \gg \bar{n}$ situation [Fig. 10(c)]:

$$\frac{v_e(z)}{v_{\text{app}}} = \frac{\cosh(\kappa z) + i\omega r'_{\text{ion}}[c'_g \cosh(\kappa z) + (c_1/\kappa)\sinh(\kappa z)]}{-[1 + (c_1/c_2)]\cosh(\kappa L_{\text{bulk}}) - (c^{\delta'}/\kappa c_2)\sinh(\kappa L_{\text{bulk}}) + i\omega r'_{\text{ion}}\{-c'_g[1 + (c_1/c_2)]\cosh(\kappa L_{\text{bulk}}) + (-(c_1/\kappa) - (c^{\delta'}c'_g/\kappa c_2))\sinh(\kappa L_{\text{bulk}})\}} + 1 \quad \text{(C11)}$$

$$\frac{v_e(z, \ \omega \to 0)}{v_{\text{app}}} \approx 1 - \frac{1}{1 + (c_1/c_2) + (c^{\delta'}/c_2)L_{\text{bulk}}} = \frac{c_1 + c^{\delta'}L_{\text{bulk}}}{c_1 + c_2 + c^{\delta'}L_{\text{bulk}}}. \quad \text{(C12)}$$

The changes in electrostatic potential in the active layer on slow enough perturbation is not only determined by the value of c_1 and c_2, but also by the chemical capacitance between the electronic and the ionic rails $c^{\delta'}L_{\text{bulk}}$.

The impedance of the whole device can then be calculated as follows:

$$Z(\omega) = \left\{ \left(1 - \frac{v_{e,1}(\omega)}{v_{\text{app}}}\right)i\omega c_A + \frac{L}{r_{\text{rad}}} + \frac{v_{e,1}}{v_{\text{app}}}g_{\text{rec},n,\text{surf1}} + \left(1 - \frac{v_{e,1}(\omega)}{v_{\text{app}}}\right)g_{\text{rec},p,\text{surf1}} + \frac{v_{e,2}(\omega)}{v_{\text{app}}}g_{\text{rec},n,\text{surf2}} \right.$$

$$\left. + \left(1 - \frac{v_{e,2}(\omega)}{v_{\text{app}}}\right)g_{\text{rec},p,\text{surf2}} + \int_0^{L_{\text{bulk}}} \left[\frac{v_e(z,\omega)}{v_{\text{app}}}g'_{\text{rec},n} + \left(1 - \frac{v_e(z,\omega)}{v_{\text{app}}}\right)(g'_{\text{rec},p} + i\omega c_p^{\delta'})\right]dz \right\}^{-1}. \quad \text{(C13)}$$

Here, $v_{e,1}$ and $v_{e,2}$ are calculated by substituting $v_e(z)/v_{\text{app}}$ from Eq. (C8) [or its simplified forms when relevant, Eqs. (C9) and (C11)] in Eqs. (C2) and (C3).

[1] J. R. Macdonald, Impedance spectroscopy, Ann. Biomed. Eng. **20**, 289 (1992).

[2] J. Jamnik and J. Maier, Treatment of the impedance of mixed conductors equivalent circuit model and explicit approximate solutions, J. Electrochem. Soc. **146**, 4183 (1999).

[3] W. Lai and S. M. Haile, Impedance spectroscopy as a tool for chemical and electrochemical analysis of mixed conductors: A case study of Ceria, J. Am. Ceram. Soc. **88**, 2979 (2005).

[4] E. Von Hauff, Impedance spectroscopy for emerging photovoltaics, J. Phys. Chem. C **123**, 11329 (2019).

[5] G. C. Barker, Aperiodic equivalent electrical circuits for the electrolyte solution, J. Electroanal. Chem. Interfacial Electrochem. **41**, 201 (1973).

[6] T. R. Brumleve and R. P. Buck, Transmission line equivalent circuit models for electrochemical impedances, J. Electroanal. Chem. **126**, 73 (1981).

[7] J. Jamnik and J. Maier, Generalised equivalent circuits for mass and charge transport: chemical capacitance and its implications, Phys. Chem. Chem. Phys. **3**, 1668 (2001).

[8] A. E. Bumberger, A. Nenning, and J. Fleig, Transmission line revisited – the impedance of mixed ionic and electronic conductors, Phys. Chem. Chem. Phys. **26**, 15068 (2024).

[9] J. Bisquert, Theory of the impedance of electron diffusion and recombination in a thin layer, J. Phys. Chem. B **106,** 325 (2002).

[10] C.-J. Tong, L. Li, L.-M. Liu, and O. V. Prezhdo, Synergy between ion migration and charge carrier recombination in metal-halide perovskites, J. Am. Chem. Soc. **142,** 3060 (2020).

[11] X. Zhang, M. E. Turiansky, J.-X. Shen, and C. G. Van De Walle, Iodine interstitials as a cause of nonradiative recombination in hybrid perovskites, Phys. Rev. B **101,** 140101 (2020).

[12] D. Meggiolaro, S. G. Motti, E. Mosconi, A. J. Barker, J. Ball, C. Andrea Riccardo Perini, F. Deschler, A. Petrozza, and F. De Angelis, Iodine chemistry determines the defect tolerance of lead-halide perovskites, Energy Environ. Sci. **11,** 702 (2018).

[13] D. Moia, I. Gelmetti, M. Stringer, O. Game, D. Lidzey, E. Palomares, P. Calado, J. Nelson, W. Fisher, and P. R. F. Barnes, Ionic-to-electronic current amplification in hybrid perovskite solar cellsâĂŕ: ionically gated transistor- interface circuit model explains hysteresis and impedance of mixed conducting devices, Energy Environ. Sci. **12,** 1296 (2019).

[14] F. Ebadi, N. Taghavinia, R. Mohammadpour, A. Hagfeldt, and W. Tress, Origin of apparent light-enhanced and negative capacitance in perovskite solar cells, Nat. Commun. **10,** 1574 (2019).

[15] S. Taibl, G. Fafilek, and J. Fleig, Impedance spectra of Fe-doped SrTiO$_3$ thin films upon bias voltage: inductive loops as a trace of ion motion, Nanoscale **8,** 13954 (2016).

[16] J. Bisquert, L. Bertoluzzi, I. Mora-Sero, and G. Garcia-Belmonte, Theory of impedance and capacitance spectroscopy of solar cells with dielectric relaxation, drift-diffusion transport, and recombination, J. Phys. Chem. C **118,** 18983 (2014).

[17] H. Wang, A. Guerrero, A. Bou, A. M. Al-Mayouf, and J. Bisquert, Kinetic and material properties of interfaces governing slow response and long timescale phenomena in perovskite solar cells, Energy Environ. Sci. **12,** 2054 (2019).

[18] E. Ghahremanirad, A. Bou, S. Olyaee, and J. Bisquert, Inductive loop in the impedance response of perovskite solar cells explained by surface polarization model, J. Phys. Chem. Lett. **8,** 1402 (2017).

[19] E. Ghahremanirad, O. Almora, S. Suresh, A. A. Drew, T. H. Chowdhury, and A. R. Uhl, Beyond protocols: Understanding the electrical behavior of perovskite solar cells by impedance spectroscopy, Adv. Energy Mater. **13,** 2204370 (2023).

[20] A. Pockett, G. E. Eperon, N. Sakai, H. J. Snaith, L. M. Peter, and P. J. Cameron, Microseconds, milliseconds and seconds: Deconvoluting the dynamic behaviour of planar perovskite solar cells, Phys. Chem. Chem. Phys. **19,** 5959 (2017).

[21] D. A. Jacobs, H. Shen, F. Pfeffer, J. Peng, T. P. White, F. J. Beck, and K. R. Catchpole, The two faces of capacitance: New interpretations for electrical impedance measurements of perovskite solar cells and their relation to hysteresis, J. Appl. Phys. **124,** 225702 (2018).

[22] D. Moia, J. Maier, and Ion Transport, Defect chemistry, and the device physics of hybrid perovskite solar cells, ACS Energy Lett. **6,** 1566 (2021).

[23] L. J. Bennett, A. J. Riquelme, J. A. Anta, N. E. Courtier, and G. Richardson, Avoiding ionic interference in computing the ideality factor for perovskite solar cells and an analytical theory of their impedance-spectroscopy response, Phys. Rev. Appl. **19,** 1 (2023).

[24] N. Filipoiu, A. T. Preda, D.-V. Anghel, R. Patru, R. E. Brophy, M. Kateb, C. Besleaga, A. G. Tomulescu, I. Pintilie, A. Manolescu, *et al.*, Capacitive and inductive effects in perovskite solar cells: The different roles of ionic current and ionic charge accumulation, Phys. Rev. Appl. **18,** 064087 (2022).

[25] F. Fabregat-Santiago, M. Kulbak, A. Zohar, M. Vallés-Pelarda, G. Hodes, D. Cahen, and I. Mora-Seró, Deleterious effect of negative capacitance on the performance of halide perovskite solar cells, ACS Energy Lett. **2,** 2007 (2017).

[26] A. J. Riquelme, K. Valadez-Villalobos, P. P. Boix, G. Oskam, I. Mora-Seró, and J. A. Anta, Understanding equivalent circuits in perovskite solar cells. Insights from drift-diffusion simulation, Phys. Chem. Chem. Phys. **24,** 15657 (2022).

[27] G. Richardson, S. E. J. O'Kane, R. G. Niemann, T. A. Peltola, J. M. Foster, P. J. Cameron, and A. B. Walker, Can slow-moving ions explain hysteresis in the current–voltage curves of perovskite solar cells?, Energy Environ. Sci. **9,** 1476 (2016).

[28] W. Clarke, M. V. Cowley, M. J. Wolf, P. Cameron, A. Walker, and G. Richardson, Inverted hysteresis as a diagnostic tool for perovskite solar cells: Insights from the drift-diffusion model, J. Appl. Phys. **133,** 095001 (2023).

[29] W. Clarke, G. Richardson, and P. Cameron, Understanding the full zoo of perovskite solar cell impedance spectra with the standard drift-diffusion model, Adv. Energy Mater. **14,** 2400955 (2024).

[30] N. E. Courtier, J. M. Foster, S. E. J. O'Kane, A. B. Walker, and G. Richardson, Systematic derivation of a surface polarisation model for planar perovskite solar cells, Eur. J. Appl. Math. **30,** 427 (2019).

[31] D. Moia, M. Jung, Y. R. Wang, and J. Maier, Ionic and electronic polarization effects in horizontal hybrid perovskite device structures close to equilibrium, Phys. Chem. Chem. Phys. **25,** 13335 (2023).

[32] D. Moia and J. Maier, Ionic and electronic energy diagrams for hybrid perovskite solar cells, Mater. Horiz. **10,** 1641 (2023).

[33] S. M. Sze and K. K. Ng, *Physics of Semiconductor Devices*, 3rd ed. (Wiley-Interscience, Hoboken, NJ, 2007).

[34] J. Nelson, *The Physics of Solar Cells* (Imperial College London, London, 2003).

[35] W. Shockley and W. T. Read, Statistics of the recombinations of holes and electrons, Phys. Rev. **87,** 835 (1952).

[36] R. N. Hall, Electron-hole recombination in germanium, Phys. Rev. **87,** 387 (1952).

[37] P. Calado, D. Burkitt, J. Yao, J. Troughton, T. M. Watson, M. J. Carnie, A. M. Telford, B. C. O'Regan, J. Nelson, and P. R. F. Barnes, Identifying dominant recombination

mechanisms in perovskite solar cells by measuring the transient ideality factor, Phys. Rev. Appl. **11**, 044005 (2019).

[38] W. Tress, M. Yavari, K. Domanski, P. Yadav, B. Niesen, J. P. Correa Baena, A. Hagfeldt, and M. Graetzel, Interpretation and evolution of open-circuit voltage, recombination, ideality factor and subgap defect states during reversible light-soaking and irreversible degradation of perovskite solar cells, Energy Environ. Sci. **11**, 151 (2018).

[39] See Supplemental Material at http://link.aps.org/supplemental/10.1103/PhysRevApplied.23.014055 for notes on the use of bipolar transistors as equivalent circuit element, approximations for the recombination and generation transconductance, the small-perturbation model of Auger recombination, complete model for devices with ion blocking contacts, approximations to the transistor recombination circuit model in a semiconductor, differential problems to the approximated circuit models, discussion on transistor-based equivalent circuit models for interfacial behavior, steady-state electronic charge concentration in mixed conducting solar cells, approximated chemical capacitance network for mixed conductors under bias, impedance calculation using MATLAB codes, input parameters for impedance calculations, discussion and interpretation of bias-dependent impedance, construction of the discretized equivalent circuit model and MATLAB codes.

[40] A. Marunchenko, J. Kumar, A. Kiligaridis, S. M. Rao, D. Tatarinov, I. Matchenya, E. Sapozhnikova, R. Ji, O. Teschow, J. Brunner, *et al.*, Charge trapping and defect dynamics as origin of memory effects in metal halide perovskite memlumors, J. Phys. Chem. Lett. **15**, 6256 (2024).

[41] W. Lai and S. M. Haile, Electrochemical impedance spectroscopy of mixed conductors under a chemical potential gradient: a case study of Pt|SDC|BSCF, Phys. Chem. Chem. Phys. **10**, 865 (2008).

[42] J. Maier, *Physical Chemistry of Ionic Materials: Ions and Electrons in Solids*, 2nd ed. (Wiley, 2022).

[43] S. Ravishankar, Z. Liu, Y. Wang, T. Kirchartz, and U. Rau, How charge carrier exchange between absorber and contact influences time constants in the frequency domain response of perovskite solar cells, Phys. Rev. X **2**, 1 (2023).

[44] W. Xu, L. J. F. Hart, B. Moss, P. Caprioglio, T. J. Macdonald, F. Furlan, J. Panidi, R. D. J. Oliver, R. A. Pacalaj, M. Heeney, *et al.*, Impact of interface energetic alignment and mobile ions on charge carrier accumulation and extraction in p-i-n perovskite solar cells, Adv. Energy Mater. **13**, 2301102 (2023).

[45] I. Mora-Seró, G. Garcia-Belmonte, P. P. Boix, M. A. Vázquez, and J. Bisquert, Impedance spectroscopy characterisation of highly efficient silicon solar cells under different light illumination intensities, Energy Environ. Sci. **2**, 678 (2009).

[46] J. Bisquert, Influence of the boundaries in the impedance of porous film electrodes, Phys. Chem. Chem. Phys. **2**, 4185 (2000).

[47] Y. Y. Proskuryakov, K. Durose, M. K. Al Turkestani, I. Mora-Seró, G. Garcia-Belmonte, F. Fabregat-Santiago, J. Bisquert, V. Barrioz, D. Lamb, S. J. C. Irvine, *et al.*, Impedance spectroscopy of thin-film CdTe/CdS solar cells under varied illumination, J. Appl. Phys. **106**, 044507 (2009).

[48] D. Moia, I. Gelmetti, P. Calado, Y. Hu, X. Li, P. Docampo, J. De Mello, J. Maier, J. Nelson, and P. R. F. Barnes, Dynamics of internal electric field screening in hybrid perovskite solar cells probed using electroabsorption, Phys. Rev. Appl. **18**, 044056 (2022).

[49] N. E. Courtier, J. M. Cave, J. M. Foster, A. B. Walker, and G. Richardson, How transport layer properties affect perovskite solar cell performance: insights from a coupled charge transport/ion migration model, Energy Environ. Sci. **12**, 396 (2019).

[50] D. A. Jacobs, Y. Wu, H. Shen, C. Barugkin, F. J. Beck, T. P. White, K. Weber, and K. R. Catchpole, Hysteresis phenomena in perovskite solar cells: the many and varied effects of ionic accumulation, Phys. Chem. Chem. Phys. **19**, 3094 (2017).

[51] I. Yokota, On the theory of mixed conduction with special reference to the conduction in silver sulfide group semiconductors, J. Phys. Soc. Jpn. **16**, 2213 (1961).

[52] T. Yang, G. Gregori, N. Pellet, M. Grätzel, and J. Maier, The significance of ion conduction in a hybrid organic–inorganic lead-iodide-based perovskite photosensitizer, Angew. Chem. **127**, 8016 (2015).

[53] A. Senocrate and J. Maier, Solid-state ionics of hybrid halide perovskites, J. Am. Chem. Soc. **141**, 8382 (2019).

[54] M. Morgenbesser, A. Schmid, A. Viernstein, J. d, D. Sirvent, F. Chiabrera, N. Bodenmüller, S. Taibl, M. Kubicek, F. Baiutti, A. Tarancon, *et al.*, SrTiO₃ based high temperature solid oxide solar cells: Photovoltages, photocurrents and mechanistic insight, Solid State Ionics **368**, 115700 (2021).

[55] G. Walch, B. Rotter, G. C. Brunauer, E. Esmaeili, A. K. Opitz, M. Kubicek, J. Summhammer, K. Ponweiser, and J. Fleig, A solid oxide photoelectrochemical cell with UV light-driven oxygen storage in mixed conducting electrodes, J. Mater. Chem. A **5**, 1637 (2017).

[56] J. Maier, Chemical resistance and chemical capacitance, Z. Naturforsch. B **75**, 15 (2020).

[57] P. Calado, I. Gelmetti, B. Hilton, M. Azzouzi, J. Nelson, and P. R. F. Barnes, Driftfusion: An open source code for simulating ordered semiconductor devices with mixed ionic-electronic conducting materials in one dimension, J. Comput. Electron. **21**, 960 (2022).

[58] C.-C. Chen and J. Maier, Space charge storage in composites: Thermodynamics, Phys. Chem. Chem. Phys. **19**, 6379 (2017).